Submitted to the Astrophysical Journal on January 18, 2006; Accepted July 10, 2006
Preprint typeset using LaTeX style emulateapj v. 6/22/04

THE X-RAY PROPERTIES OF ACTIVE GALACTIC NUCLEI WITH DOUBLE-PEAKED BALMER LINES

Iskra V. Strateva[1,2], W. N. Brandt[1], Michael Eracleous[1], Donald P. Schneider[1], George Chartas[1]

Submitted to the Astrophysical Journal on January 18, 2006; Accepted July 10, 2006

ABSTRACT

Double-peaked Balmer-line profiles originate in the accretion disks of a few percent of optically selected AGN. The reasons behind the strong low-ionization line emission from the accretion disks of these objects is still uncertain. In this paper, we characterize the X-ray properties of 39 double-peaked Balmer line AGN, 29 from the Sloan Digital Sky Survey and 10 low optical-luminosity double-peaked emitters from earlier radio-selected samples. We find that the UV-to-X-ray slope of radio-quiet (RQ) double-peaked emitters as a class does not differ substantially from that of normal RQ AGN with similar UV monochromatic luminosity. The radio-loud (RL) double-peaked emitters, with the exception of LINER galaxies, are more luminous in the X-rays than RQ AGN, as has been observed for other RL AGN with single-peaked profiles. The X-ray spectral shapes of double-peaked emitters, measured by their hardness ratios or power-law photon indices, are also largely consistent with those of normal AGN of similar radio-loudness. In practically all cases studied here, external illumination of the accretion disk is necessary to produce the Balmer-line emission, as the gravitational energy released locally in the disk by viscous stresses is insufficient to produce lines of the observed strength. In the Appendix we study the variability of Mrk 926, a double-peaked emitter with several observations in the optical and X-ray bands.

Subject headings: Galaxies: Active: Nuclei, Galaxies: Active: Optical/UV/X-ray, Galaxies: Active: Evolution, Methods: Statistical

1. INTRODUCTION

A small class of Active Galactic Nuclei (AGN) emit broad, double-peaked, low-ionization lines, which most likely originate directly from the AGN accretion disk. The frequency of double-peaked lines is high (∼20%) among the radio-loud equivalents of Seyfert galaxies, broad-line radio galaxies (BLRG; Eracleous & Halpern 1994, 2003), and much lower (∼3%) among the general population of low-redshift, optically selected AGN (Strateva et al. 2003, hereafter S03). The class of double-peaked emitters is diverse — it includes both radio-loud (RL) and radio-quiet (RQ) AGN with luminosities ranging from low-luminosity low-ionization nuclear emission-line region (LINER) galaxies to low-luminosity quasars. The optical spectra of double-peaked emitters are sometimes dominated by the featureless continuum of the AGN, but in a significant fraction of cases starlight from the host galaxy makes a dominant contribution to the observed optical continuum. The handful of double-peaked emission-line BLRG with reliable black-hole mass measurements (10 black hole masses measured via the Ca II triplet velocity dispersion and the relation between stellar velocity dispersion and black-hole mass; Lewis & Eracleous 2006) have $0.4 \times 10^8 M_\odot < M_{\rm BH} < 5 \times 10^8 M_\odot$ and range from low-to-moderate Eddington-ratio AGN ($10^{-5} < L_{\rm bol}/L_{\rm Edd} < 10^{-1}$).

A large fraction of the originally studied double-peaked emitters were associated with low optical luminosity AGN. The Sloan Digital Sky Survey (SDSS, York et al. 2000) sample, which increased the number of medium-luminosity AGN (see Figure 1), also showed that the optical luminosity distributions of double-peaked emitters and normal AGN at $z \lesssim 0.3$ are not substantially different. This suggests that the apparent lack of double-peaked emitters among the most optically luminous AGN is a selection effect related to the rarity of very luminous sources and the small volume of space considered to date. The large range of Eddington ratios observed

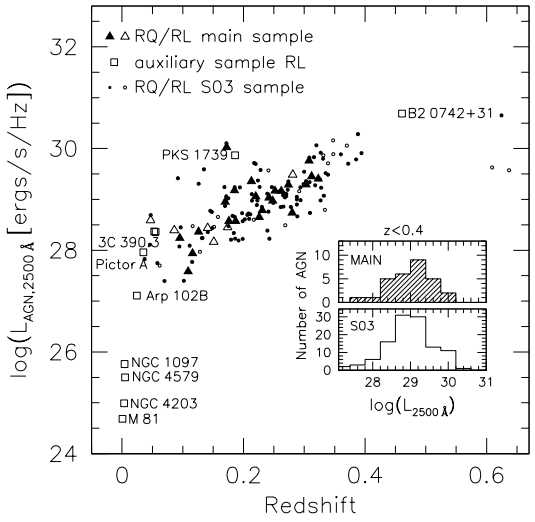

Fig. 1.— Redshift vs. 2500 Å monochromatic luminosity (corrected for starlight). The main SDSS double-peaked sample is shown with triangles, the S03 sample with small circles, and the auxiliary sample with open squares. Open symbols denote the RL AGN. The $z < 0.4$ monochromatic-luminosity histograms for the main sample (hatched histogram) and the S03 (open histogram) samples are given as an inset, showing no significant difference in the two distributions.

[1] Department of Astronomy and Astrophysics, 525 Davey Lab, Pennsylvania State University, University Park, PA 16802
[2] Max-Planck-Institut für extraterrestrische Physik, Postfach 1312, 85741 Garching, Germany

in AGN with double-peaked emission lines together with their large range of luminosities (which probably translates into a large range of Eddington ratios) suggest that the existence of strong Balmer-line emission from the accretion disks of AGN is either independent of the Eddington ratio of the source, or that there are different explanations for the presence of double-peaked Balmer lines in AGN with different Eddington ratios. In addition to a large range of Eddington ratios, the known double-peaked emitters tend to have broader Balmer lines ($\approx 5\times$ the full width at half maximum of normal AGN) and stronger low-ionization narrow lines (e.g., [O I] 6300Å) than similar AGN without double-peaked lines. As a class, the double-peaked emitters possess a diverse set of optical/UV properties but most do not appear remarkably different in their other properties from the general AGN population.

Based on the prototype double-peaked emitter, Arp 102B, and the initial sample of double-peaked BLRG and LINER galaxies, there were reasons to believe that disk emission in AGN is associated with low-luminosity, low Eddington-ratio accretion in which the inner parts of the accretion disk (less than a few tens of gravitational radii, R_g) became geometrically thick and optically thin (e.g., Narayan et al. 1998), emitting energetic X-rays which illuminate the outer (outside a few hundred gravitational radii) regions of the disk (Chen & Halpern 1989; Nagao et al. 2002; Eracleous & Halpern 2003). Since most of the initially known double-peaked emitters had strong Balmer lines, which could not have been produced by the release of gravitational energy locally without invoking an unrealistic radiative efficiency, the X-ray illumination from the thick inner disk was necessary to produce strong disk-emission signatures.

The theoretical model presented above remains the best explanation for low-ionization broad-line disk emission in low-luminosity, low Eddington-ratio AGN. In its original form, however, it is not applicable to higher Eddington-ratio (and luminosity) double-peaked emitters. As the Eddington ratio and luminosity of the AGN increases, the structure of the inner disk and the illumination pattern of the outer disk change. In addition, line-driven winds could become important, filling-in the low-velocity minima of the double-peaked emission lines until the profiles are effectively single peaked (e.g., Murray & Chiang 1997; Proga et al. 2000). If we can establish clearly the need for external illumination in higher luminosity (and presumably Eddington ratio) sources, we can revise the theoretical picture of their central regions by exploring evidence for the presence of a different kind of disk-illuminating structure — for example — a "flared" disk, a scattering corona, vertically extended wind, or a radiation supported torus.

In search of clues that might reveal the mechanism responsible for the existence of double-peaked Balmer lines in AGN, we decided to study in more detail the 0.5–10 keV X-ray properties of this class. If additional illumination is necessary to produce significant disk line-emission signatures in AGN, their high-energy emission and their overall spectral energy distributions might be expected to differ from those of single-peaked AGN. S03 and Wu & Liu (2004) calculated the UV-to-X-ray slopes ($\alpha_{\rm ox}$) of double-peaked emitters with *ROSAT* All Sky Survey (RASS, Voges 1993) detections and concluded that they do not differ strongly from those of other AGN. These rough comparisons, however, included only X-ray detected subsamples of double-peaked emitters, which are not representative of the full double-peaked Sloan Digital Sky Survey sample and the general double-peaked line population. They also did not take into account the dependence of $\alpha_{\rm ox}$ on AGN luminosity (e.g., Strateva et al. 2005; Steffen et al. 2006).

In this paper we present a detailed investigation of the X-ray properties (soft X-ray luminosities, UV-to-X-ray slopes, X-ray power-law photon indices, and X-ray absorption whenever available) of a sample of double-peaked emitters serendipitously included in pointed *ROSAT*, *XMM-Newton*, and *Chandra* observations. The paper is organized as follows: the sample of double-peaked emitters with X-ray observations is presented in § 2, followed by the study of their UV-to-X-ray slopes and X-ray spectral shapes in § 3. § 4 discusses the evidence for external illumination, followed by the summary and conclusions in § 5. In the Appendix we comment on the variability of Mrk 926, a double-peaked emitter from our sample with several optical and X-ray observations. Throughout this work we use the *Wilkinson Microwave Anisotropy Probe* cosmology parameters from Spergel et al. (2003) to compute the luminosities of AGN: $\Omega_\Lambda = 0.73$, flat cosmology, with H_0=72 km s^{-1} Mpc^{-1}.

2. SAMPLE SELECTION

Our sample consists of 29 double-peaked emitters selected from the SDSS and serendipitously observed or previously targeted by *ROSAT*, *XMM-Newton*, or *Chandra* (hereafter the main sample). We add to this sample 10 BLRG, LINER galaxies, and RL quasars with good UV and X-ray observations (hereafter the auxiliary sample). A total of 16 of the 39 double-peaked emitters are RL (6 main-sample objects and 10 auxiliary sample objects), and the remaining 23 (main-sample objects) are RQ.

2.1. *The Main Sample of Double-Peaked Emitters*

In order to increase the number of SDSS double-peaked emitters with sensitive X-ray observations, we start with a sample of SDSS AGN[3] with $z < 0.4$ (which guarantees that the Hα line is observed) selected from Data Release 3 (DR3, Abazajian et al. 2005) which fall in pointed *ROSAT*, *XMM-Newton*, or *Chandra* observations that are publicly available. The effective exposure times (i.e., after accounting for the off-axis angle, X-ray background flares, etc.) of these observations are all > 1 ks and are > 2 ks for 80% of the objects; the median exposure time is 4.2 ks. Using SDSS-RASS matches would have substantially increased our sample size but decreased our detection fraction and the total X-ray counts of detected objects (limiting our ability to extract X-ray spectral information). Using only the S03 double-peaked emitter sample, which was selected from SDSS observations performed prior to March 2003, would have decreased the

[3] Here the term AGN is not restricted to represent the SDSS quasar sample presented by Schneider et al. (2005); it stands for all objects showing broad Balmer lines, including those originally targeted as galaxies by the SDSS.

number of sources, thus weakening the significance of our statistical inferences.

Since the double-peaked emitters are a subsample of the asymmetric broad-line AGN (see S03 for more details), we start by selecting a subsample of the SDSS AGN with *ROSAT*, *XMM-Newton*, or *Chandra* observations and asymmetric broad Hα emission lines. We fit the Hα line region of each spectrum[4] with a combination of Gaussians. These Gaussian representations of the Hα line region allow us to isolate the broad Hα line component (excluding the narrow Hα, [N II], and [S II] lines) and to select the AGN with double-peaked broad lines. In addition, obtaining a smooth representation of the broad Hα line component allows easy measurement of a set of model-independent parameters: (1) the rest-frame full width at half maximum, FWHM, (2) the rest-frame full width at quarter maximum, FWQM, (3,4) the centroids of the line at half and quarter maximum, FWHMc and FWQMc (measured with respect to the rest-frame narrow Hα line), (5,6) the rest wavelengths of the red and blue peaks with respect to the narrow Hα line, $\lambda_{\rm Red}$ and $\lambda_{\rm Blue}$, and (7) the peak separation, $\lambda_{\rm Red} - \lambda_{\rm Blue}$. More details on the broad-line parameter measurements and the double-peak selection criteria can be found in §3.2 of S03; the Hα line measurements for the selected objects are reported in Table 1. Eight of the resulting 29 main-sample double-peaked emitters are part of the S03 sample. For consistency with the rest of the sample, we used the newest SDSS spectroscopic reductions currently available and obtained new Hα-line parameter measurements for these eight objects. The results are consistent with those reported in the S03 paper, within the errors quoted in Table 4 of S03. The Hα-line luminosities of the eight new reductions were found to be slightly higher on the average (by $\sim$20%).

Of the 29 SDSS AGN with double-peaked lines, 22 were observed by the *ROSAT* PSPC only, five by *XMM-Newton*, and two by *Chandra*, as shown in Table 1. Whenever hard-band (above 2 keV) observations were available for double-peaked emitters in *ROSAT* PSPC fields (3 cases with both *XMM-Newton* and *ROSAT* data), we used the *XMM-Newton* data. If both *XMM-Newton* and *Chandra* data were available, we chose the observation with the larger number of photons, and compare the results from the two observatories. Four SDSS double-peaked emitters have been observed repeatedly with various X-ray satellites (see the top portion of Table 1); we use all the available X-ray data for the best example, SDSSJ 2304−0841, to study variability in Appendix A. Five of the X-ray observed double-peaked emitters have sufficient counts (100–24000 in the 2–10 keV band) to allow fitting of their X-ray spectra. Three of the objects observed by *ROSAT* are not detected in the soft (0.5–2 keV) band; for these three we derive (3σ) upper limits to the soft-band fluxes.

Four of the objects observed with *ROSAT* were the targets of their respective PSPC observations (see the top panel of Table 1). Four additional objects, for which X-ray spectra are available, were also the targets of their respective observations (see the bottom panel of Table 1).

[4] The spectra were decomposed into AGN and starlight components first (Vanden Berk et al. 2006), and both the starlight and a power-law representation of the AGN continuum were subtracted.

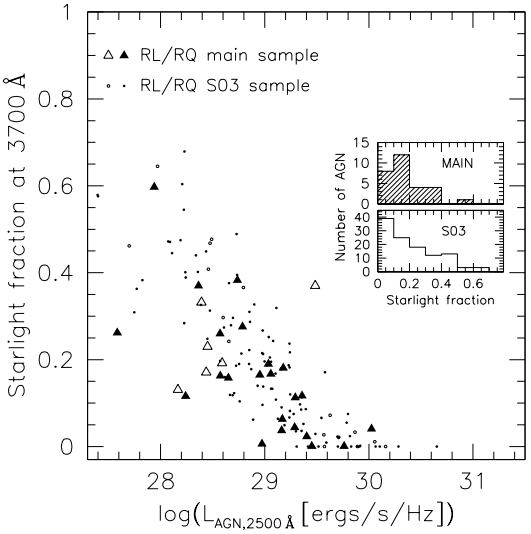

FIG. 2.— Monochromatic luminosity at 2500 Å vs. starlight fraction. Symbols are as in Figure 1. The two histograms show the distribution of starlight fractions for the main and S03 samples.

A large fraction of targeted observations could have biased the sample of X-ray observed double-peaked emitters; § 2.2 below demonstrates that this is not the case for our sample.

2.2. *Main Sample Properties*

In this section we show the basic properties of the main sample of double-peaked emitters studied here. We demonstrate that the main sample is representative of the sample of SDSS double-peaked emitters by performing a series of one- and two-dimensional statistical comparisons with the SDSS sample from S03 (hereafter, the S03 sample[5]). We use Kolmogorov-Smirnov (K-S) tests which measure the maximum distance, D, between two cumulative distributions, and compute the null hypothesis probability that the data sets are drawn from the same distribution, P. Small values of D and large values of P indicate that the observed data are highly probable given the null hypothesis; we will consider this sufficient evidence that the X-ray observed AGN are representative of the S03 sample. For more details on the "two-dimensional K-S test", see Peacock (1983).

2.2.1. *Monochromatic Luminosity and Redshift Distributions*

Using the starlight-subtracted monochromatic flux measurement at a rest-frame wavelength of 3700 Å (the bluest wavelength observed for all SDSS AGN, irrespective of their redshift), we can estimate the monochromatic flux at rest-frame 2500 Å, which is a convenient measure of brightness commonly used, for example, to compute the UV-to-X-ray index. We assumed that the optical/UV flux is a power-law function of wavelength in the 2500–3700 Å region ($f_\lambda \propto \lambda^{\alpha_\lambda}$) with an index of

[5] We exclude the three $z \approx 0.6$ S03 double-peaked emitters from the quantitative comparisons presented here, since they lie outside the standard Hα selection region and were included in the S03 sample after being discovered serendipitously. See S03 for more details.

TABLE 1
MAIN SAMPLE: Hα-LINE MEASUREMENTS AND 0.5–2 keV LUMINOSITIES

Object (1)	z (2)	$L_{\rm H\alpha}$ (3)	$L_{0.5-2\,\rm keV}$ (4)	FWQM (5)	FWQMc (6)	FWHM (7)	FWHMc (8)	$\lambda_{\rm Red}$ (9)	$\lambda_{\rm Blue}$ (10)
004319.75+005115.3	0.3081	17	180	14600	10	11900	−210	3200	−3400
005709.93+144610.3	0.1722	35	240	12900	1230	9570	1010	2300	−1010
022417.17−092549.3	0.3115	12	84	9800	90	7160	270	1860	−240
081329.29+483427.9	0.2737	10	90	11800	−190	8610	−530	1350	−1970
091828.60+513932.1	0.1854	6.2	8.2	6350	−20	4820	−70	560	−940
092108.63+453857.4	0.1744	1.5	87	17120	−3520	9270	−1320	130	−3590
092813.25+052622.5	0.1874	4.3	18	13800	690	9660	920	3180	1200
093844.46+005715.8	0.1704	31	37	11900	230	8250	−40	2820	−580
094215.13+090015.8	0.2126	11	18	42700	4380	36900	3020	20100	−12400
094745.15+072520.6	0.0858	5.2	3.1	15400	−980	9190	−240	−770	−6630
095427.61+485638.1	0.2481	4.5	25	15100	380	8520	−500	6150	−2460
095802.84+490311.1	0.2416	4.9	22	7800	90	5760	−100	640	−1000
104132.78−005057.5	0.3029	9.6	120	10600	1000	7340	1180	1020	−1290
110109.58+512207.1	0.2521	4.2	22	12000	420	9260	420	1960	−620
111121.71+482046.0	0.2809	10	31	23800	710	18800	260	6670	−3980
113450.99+491208.9	0.1765	1.6	2.6	9850	−190	6530	−280	−110	−1960
114454.86+560238.2	0.2310	3.0	29	10900	970	8310	670	3470	−1000
114719.22+003351.2	0.2624	7.1	<10	9170	−160	6830	−160	1500	−1380
115038.86+020854.2	0.1095	0.41	3.1	8950	270	7080	−40	320	−2100
115741.94−032106.1	0.2195	3.1	<7.3	11600	−170	8890	−50	1920	−1670
120848.82+101342.6	0.1158	0.62	21	9450	−10	7350	330	2410	−150
130723.13+532318.9	0.3231	8.0	110	10200	−120	7990	−170	1950	−1950
132355.69+652233.0	0.2261	1.6	5.8	7610	100	5720	460	2910	−40
144302.76+520137.2	0.1412	3.2	73	9170	−70	5830	−470	3280	−520
161742.53+322234.3	0.1500	12	6.2	23300	1150	19600	840	7400	−5490
164031.86+373437.2	0.2796	3.1	56	6790	−400	4970	−800	−10	−2030
170102.29+340400.6	0.0946	3.0	8.0	7910	−260	5800	−450	−90	−1760
213338.42+101923.6	0.1257	1.4	<2.2	10400	280	7970	30	2270	−1980
230443.47−084108.6	0.0469	4.8	85	11400	−1210	8790	−970	1560	−1620

NOTE. — (1) the SDSS name given in the J2000 epoch RA and Dec form, HHMMSS.ss±DDMMSS.s; (2) redshift; (3) Hα line luminosity in units of $10^{42}\,\rm erg\,s^{-1}$; (4) rest-frame 0.5–2 keV luminosity in units of $10^{42}\,\rm erg\,s^{-1}$, estimated from the observed 0.5–2 keV band for the 22 *ROSAT* objects (assuming $\Gamma = 2$) and estimated from the spectral fits for the 7 *XMM-Newton* and *Chandra* observed objects, including corrections for any intrinsic absorption; (5) the FWQM of the Hα line, in $\rm km\,s^{-1}$; (6) the FWQM centroid in $\rm km\,s^{-1}$; (7) the FWHM of the Hα line, in $\rm km\,s^{-1}$; (8) the FWHM centroid in $\rm km\,s^{-1}$; (9) the position of the red peak, $\lambda_{\rm Red}$, with respect to the narrow Hα line, in $\rm km\,s^{-1}$; (10) the position of the blue peak, $\lambda_{\rm Blue}$, with respect to the narrow Hα line, in $\rm km\,s^{-1}$. Positive velocities denote a redshift.

$\alpha_\lambda = -1.5$ (Vanden Berk et al. 2001). Figure 1 shows the redshift vs. log of the 2500 Å monochromatic luminosity ($l_{2500\rm Å} = \log[L_{2500\rm Å}(\rm erg\,cm^{-2}\,s^{-1}\,Hz^{-1})]$) diagram for the main SDSS and auxiliary double-peaked samples in comparison to the S03 sample. The correlation between redshift and luminosity in flux-limited samples is obvious for both the S03 and the main samples; in addition, the double-peaked emitters from the main sample follow the luminosity-redshift trend of the S03 sample. As shown in the inset histograms in Figure 1, the monochromatic luminosities of the main and S03 samples are indistinguishable, which is confirmed by a one-dimensional K-S test ($D = 0.15$, $P = 65\%$). The redshift distribution of the main sample of double-peaked emitters is also similar to that of the S03 sample ($D = 0.17$, $P = 47\%$). The two-dimensional (luminosity-redshift) K-S test gives a similar result, with $D = 0.17$ and $P = 57\%$. These results remain qualitatively the same if we repeat the test for the RQ subsamples.

There are six RL AGN out of a total of 29 AGN (21%) in the main SDSS double-peaked sample, compared to 15 out of 113 (13%) in the similar-redshift ($z < 0.4$) S03 sample. A Fisher exact test confirms that the difference is not statistically significant, with a chance probability of 38%. A careful examination of Figure 1 reveals that five of the six RL objects in our main sample occupy the lowest redshift and UV luminosity corner of the diagram. Performing a two-dimensional K-S test for the RL subsamples of the main and S03 samples returns $D = 0.47$ and $P = 23\%$. The distance between the RL distributions is substantial, but not statistically significant.

2.2.2. *Starlight Fraction*

Figure 2 shows the starlight fractions (measured at rest-frame 3700 Å) of the main-sample double-peaked emitters in comparison with those of the S03 sample. As a class, RL double-peaked emitters were found to have larger starlight contributions to the continuum around Hα than other RL AGN. A one-dimensional K-S test returns a small distance ($D = 0.15$) which is not statistically significant ($P = 63\%$). A two-dimensional (starlight fraction-luminosity) K-S test returns a larger distance ($D = 0.28$) which is also not statistically significant ($P = 9\%$).

2.2.3. *Model-Independent Line Measurements*

In addition to luminosity, redshift, and starlight-fraction distribution comparisons, we also compare the Hα line profiles of the main-sample AGN with those of

TABLE 2
X-ray Observations

Object (1)	Observatory (2)	ObsID (3)	Instrument (4)	ObsDate (5)	$t_{\rm exp}$ (6)	Comments (7)
022417.17−092549.3	*ROSAT*	rp800016n00	PSPC	18/01/92	13.6	
081329.29+483427.9	*ROSAT*	rp700249n00	PSPC	01/04/91	6.5	
092108.63+453857.4	*ROSAT*	rp700539n00	PSPC	03/05/92	4.3	Target
092813.25+052622.5	*ROSAT*	rp200466n00	PSPC	12/05/92	3.7	
094215.13+090015.8	*ROSAT*	rp800481n00	PSPC	03/11/93	1.1	
094745.15+072520.6	*ROSAT*	rp701587n00	PSPC	04/11/93	11.0	Target
095427.61+485638.1	*ROSAT*	rp700046n00	PSPC	13/04/91	3.5	
095802.84+490311.1	*ROSAT*	rp700150a02	PSPC	20/10/93	1.9	
104132.78−005057.5	*ROSAT*	rp800194n00	PSPC	04/06/92	7.2	
110109.58+512207.1	*ROSAT*	rf201357n00	PSPC	29/11/92	2.1	
114454.86+560238.2	*ROSAT*	rp800106n00	PSPC	19/11/91	4.9	
114719.22+003351.2	*ROSAT*	rp201242n00	PSPC	23/06/92	5.8	
115038.86+020854.2	*ROSAT*	rp200813n00	PSPC	02/06/92	7.7	
115741.94−032106.1	*ROSAT*	rp201367n00	PSPC	07/07/92	3.3	
120848.82+101342.6	*ROSAT*	rp700079a01	PSPC	03/06/92	3.0	
130723.13+532318.9	*ROSAT*	rp300394n00	PSPC	10/11/93	12.0	
132355.69+652233.0	*ROSAT*	rp700803n00	PSPC	30/11/92	8.4	
144302.76+520137.2	*ROSAT*	rp701408n00	PSPC	13/07/93	6.8	Target
161742.53+322234.3	*ROSAT*	rp701589n00	PSPC	18/08/93	10.1	3C 332, Target
164031.86+373437.2	*ROSAT*	rp800503n00	PSPC	31/07/93	5.2	
170102.29+340400.6	*ROSAT*	rp201079n00	PSPC	02/09/92	6.4	
213338.42+101923.6	*ROSAT*	rp701252n00	PSPC	29/05/93	18.6	
004319.75+005115.3	*XMM-Newton*	0090070201	PN/MOS	04/01/02	16.3	UM 269, Target
...	*ASCA*	75020000	GIS/SIS	13/07/97	31.8	UM 269, Target
...	*ROSAT*	rp700377	PSPC	30/12/91	5.1	UM 269
005709.93+144610.3	*Chandra*	00865N002	ACIS-S7	28/07/00	4.7	Target, pileed-up
091828.60+513932.1	*XMM-Newton*	0084230601	PN/MOS	26/04/01	16.0	
...	*Chandra*	00533N001	ACIS-I1	05/09/00	11.3	
093844.46+005715.8	*Chandra*	04035N001	ASIS-S2	02/01/03	1.4	Target
111121.71+482046.0	*XMM-Newton*	0104861001	PN/MOS	01/06/02	27.4	
...	*XMM-Newton*	0059750401	PN/MOS	26/04/02	29.2*	flaring background
...	*ROSAT*	rp700297n00	PSPC	15/05/92	3.1	
113450.99+491208.9	*XMM-Newton*	0149900201	PN/MOS	24/11/03	17.9	
230443.47−084108.6	*XMM-Newton*	0109130701	PN/MOS	01/12/00	7.3	MCG-2-58-22, Mrk 926, Target
...	*ASCA*	75049010	GIS/SIS	15/12/97	102.7	MCG-2-58-22, Mrk 926, Target
...	*ASCA*	75049000	GIS/SIS	01/06/97	104.9	MCG-2-58-22, Mrk 926, Target
...	*ASCA*	70004000	GIS/SIS	25/05/93	85.6	MCG-2-58-22, Mrk 926, Target
...	*ROSAT*	rp701364	PSPC	01/12/93	2.16	MCG-2-58-22, Mrk 926
...	*ROSAT*	rp700998	PSPC	24/05/93	10.2	MCG-2-58-22, Mrk 926
...	*ROSAT*	rp701250	PSPC	21/05/93	18.1	MCG-2-58-22, Mrk 926
...	*ROSAT*	rp700107	PSPC	21/11/91	3.37	MCG-2-58-22, Mrk 926
...	*ROSAT*	rs931862	PSPC	21/11/90	0.314	MCG-2-58-22, Mrk 926
...	*ROSAT*	rs931962	PSPC	18/11/90	0.314	MCG-2-58-22, Mrk 926

Note. — (1) SDSS name given in the J2000 epoch RA and Dec form, HHMMSS.ss±DDMMSS.s; (2) Observatory name; (3) Observation ID; (4) Instrument; (5) Date of the observation in a dd/mm/yy format; (6) Effective exposure time, $t_{\rm exp}$, in ks, except in the case of the second SDSSJ 111121.71+482046.0 *XMM-Newton* exposure (denoted by *); this exposure is fully flared and the quoted $t_{\rm exp}$ includes the time lost due to flaring; (7) Alternative names and comments.

S03, using the broad-line parameter measurements described in § 2.1. Figure 3 shows the distribution of peak separations vs. FWQM measurements for the main and S03 samples. As described in §6 of S03, the peak separation is largely determined by the outer radius of the disk emission region for axisymmetric disks, while the FWQM is determined by the disk inclination and inner radius of emission. Quantitative comparison of the two samples using a two-dimensional K-S test shows no evidence that the two samples are significantly different (with $D = 0.18$ and $P = 54\%$).

Figure 4 shows binned distributions of the FWQM and the FWQM centroid for the main and S03 samples of double-peaked emitters (as in Fig. 10 of S03, the histograms of the parent sample of all AGN with $z \lesssim 0.3$ are also shown). In both cases a one-dimensional K-S test suggests that the (unbinned) distributions of the main and S03 samples of double-peaked emitters are indistinguishable ($D \approx 0.11$, $P \approx 90\%$).

2.2.4. *Axisymmetric Model Disk Fits*

We attempted to fit all the X-ray observed SDSS AGN with double-peaked lines with an axisymmetric disk-emission model (Chen & Halpern 1989). Six of the 29 AGN (∼17%) allow acceptable axisymmetric disk fits (i.e. we reject fits with correlated residuals), two of which are shown in Figure 5. The emission-region parameters for these six objects are given in Table 1. Two double-peaked emitters, SDSSJ 0918+5139 and SDSSJ 1134+4912, with $\xi_1 = 100\,R_G$ in Table 1, have poorly constrained inner radii; the only evidence for a small inner radius in these AGN comes from an ex-

TABLE 3
Axisymmetric Disk Fits

Object (1)	i° (2)	q (3)	ξ_1 (4)	ξ_2 (5)	σ (6)	$F_{\lambda,o}$ (7)	$F_{\mathrm{H}\alpha}$ (8)
091828.60+513932.1	25	2	100	9150	495	3.0E-4	5.5
111121.71+482046.0	36	3	190	2200	2000	6.5	3.2
113450.99+491208.9	32	2	100	5530	620	1.1E-4	1.6
114454.86+560238.2	16	3	210	2190	980	3.3	1.5
115741.94−032106.1	26	2	230	3450	900	6.7E-3	1.9
130723.13+532318.9	27	2	330	4260	760	6.6E-3	1.7

Note. — Axisymmetric disk fits following Chen & Halpern (1989). The inclination (col. 2) is in degrees; the illumination power-law slope, q (3); the inner (4) and outer (5) radii are in gravitational radii (R_G); the turbulent velocity (6) is in $\mathrm{km\,s^{-1}}$; the flux-density normalization (7) is in units of $10^{-17}\,\mathrm{erg\,cm^{-2}\,s^{-1}\,\AA^{-1}}$; the H$\alpha$ line flux (8) is in units of $10^{-14}\,\mathrm{erg\,cm^{-2}\,s^{-1}}$.

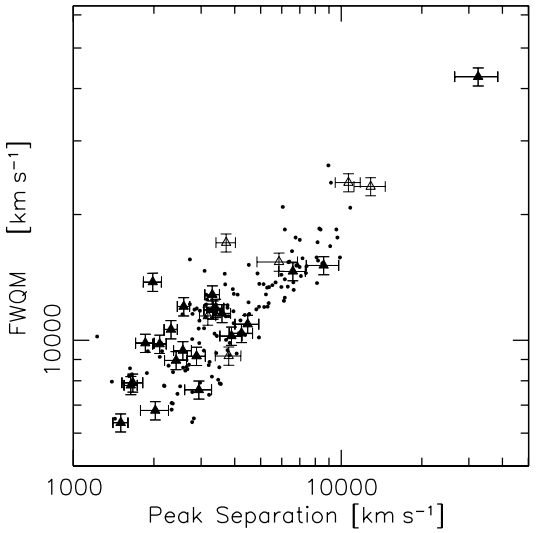

Fig. 3.— Broad Hα line parameter comparison: peak separation vs. FWQM for the main-sample double-peaked emitters (large open/solid triangles with error bars for RL/RQ AGN) and the S03 sample (solid circles). The error bars (which include uncertainties due to both measurement error and variability) were estimated to be ∼5% for the FWQM measurements and as much as 50% for the peak-separation measurements by S03.

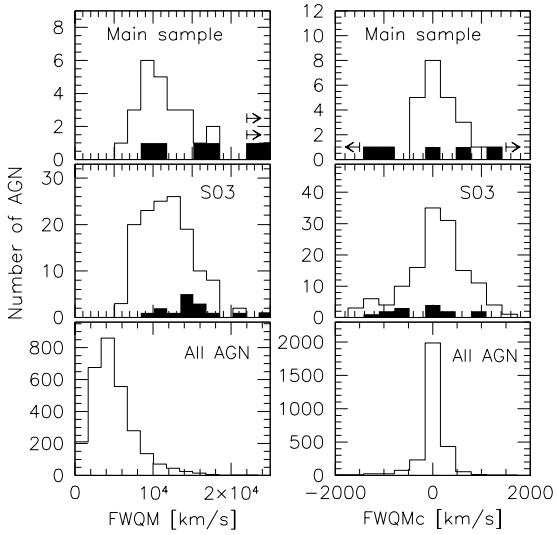

Fig. 4.— Comparison between the distributions of the Hα FWQM (left) and the FWQM centroid (right) for the X-ray observed SDSS AGN (top histograms), the S03 sample (middle histograms), and the parent sample of all SDSS AGN with $z \lesssim 0.3$ from S03 (bottom histograms). The solid histograms in the top and middle row give the contribution of RL double-peaked emitters from the main and S03 samples, respectively; the arrows indicate four main sample double-peaked emitters with values outside the displayed range.

tended blueshifted tail of the relatively narrow Hα lines, whose existence is strongly dependent on the continuum subtraction. Overall, the parameters listed in Table 1 cover the same ranges as those found by S03 and Strateva et al. (2006, in preparation) for the subsample of S03 AGN which allow axisymmetric disk fits. The fraction of double-peaked emitters with Hα line profiles consistent with emission from an axisymmetric disk is also similar to that found for the S03 sample Strateva et al. (2006, in preparation).

We conclude that the objects in our main sample are representative of the S03 sample in their luminosity, redshift, host-starlight contributions, and broad line-profile parameter distributions.

2.3. *Auxiliary Double-Peaked Sample*

In addition to the X-ray observed double-peaked sample presented above, we include for comparison purposes 10 RL AGN — two RL quasars, four BLRG, and four LINER galaxies — previously studied in the X-ray band (see Table 1). Six of these 10 AGN are part of a recently concluded program to obtain *Hubble Space Telescope* (HST) UV spectra of nearby RL double-peaked emitters with high-quality X-ray, optical, and radio observations and a large range of X-ray luminosities (Eracleous et al. 2006, in preparation). The remaining four are Arp 102B, the prototype double-peaked emitter studied in the X-ray band by Eracleous et al. (2003), and three low-luminosity LINER galaxies with archival X-ray observations — M 81, NGC 4203, and NGC 4579 (see Table 1 and associated references). An additional

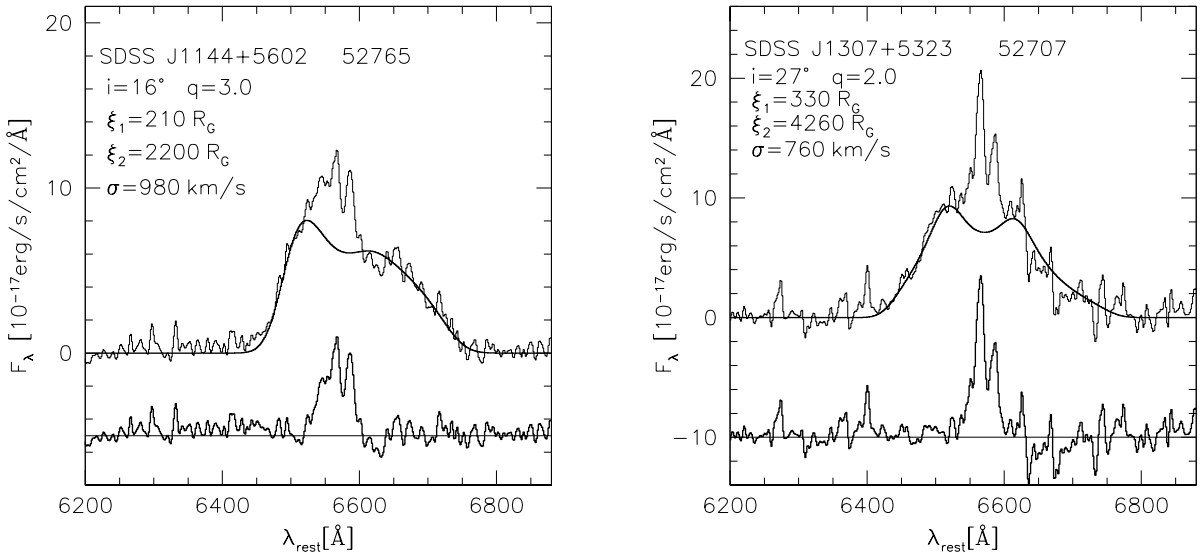

FIG. 5.— Example axisymmetric disk-model fits (solid line overlying the spectrum). The residuals, including the narrow Hα and [N II] lines, are given below, displaced on the flux scale for clarity. The SDSS name, the MJD of the observation, and the disk-model parameters (see §2.2.4 for details) are also given in the top-left corner of each panel.

BLRG with double-peaked lines from the Eracleous et al. sample, 3C 332, was independently found in the SDSS-*ROSAT* sample, and is considered a main-sample object in this paper.

Eight of these 10 double-peaked emitters have X-ray spectral fits, including estimates of X-ray power-law photon indices and absorbing column densities, as well as UV-to-X-ray slopes. When multiple X-ray observations of an object were available, we used the best observations available (longest exposures, coverage up to 10 keV, lack of pile-up). Thus for NGC 4203 we used the photon index from the spectral fit to the ~ 85 ks *ASCA* observation reported in Iyomoto et al. (1998) ($\Gamma = 1.85 \pm 0.10$), and the X-ray fluxes and flux ratios obtained from the $\sim$ 1.8 ks *Chandra* observation ($\Gamma = 1.9 \pm 0.3$ in the 2–10 keV region, assuming no intrinsic absorption). As noted by Iyomoto et al. (1998), the *ASCA* observation blends the true nuclear flux of NGC 4203 with that of another object with the same spectral shape. Our more accurate *Chandra* flux measurement in the 2–10 keV band agrees to within 20% with the flux estimate of Iyomoto et al. (1998) for the nuclear source in NGC 4203, suggesting that the object was in a similar flux state. For NGC 4579 we used a 2001 *XMM-Newton* observation (see also Dewangan et al. 2004) and confirmed that the results did not differ substantially from the 1995 *ASCA* observation which was obtained only 6 months after the UV data Terashima et al. (1998). Terashima et al. (1998) fit the full *ASCA* range with an absorbed power-law plus a Raymond-Smith model, with a photon index of $\Gamma = 1.72 \pm 0.05$, absorption consistent with the Galactic column, and a 2–10 keV flux of $4.3 \times 10^{-12}\,\mathrm{erg\,cm^{-2}\,s^{-1}}$. Using the 2001 *XMM-Newton* data we obtain a power-law fit with $\Gamma = 1.82 \pm 0.03$, $F_{2-10\,\mathrm{keV}} = 3.8 \pm 0.1 \times 10^{-12}\,\mathrm{erg\,cm^{-2}\,s^{-1}}$, and no intrinsic absorption. NGC 4579 was also observed by *ASCA* in 1998 (Terashima et al. 2000) and *Chandra* in 2000 (Eracleous et al. 2002) in a higher flux state: $F_{2-10\,\mathrm{keV}} = 5.3 \times 10^{-12}\,\mathrm{erg\,cm^{-2}\,s^{-1}}$ (1998) and $F_{2-10\,\mathrm{keV}} = 5.2 \times 10^{-12}\,\mathrm{erg\,cm^{-2}\,s^{-1}}$ (2000), as well as slightly different 2–10 keV photon index $\Gamma = 1.81 \pm 0.6$ (1998) and $\Gamma = 1.88 \pm 0.03$ (2000). For M 81 we used a 2001 *XMM-Newton* pn observation (ObsID 0111800101, 54.3 ks) and checked that the earliest 1993 *ASCA* observation (Ishisaki et al. 1996), which was closer in time to the UV observation, gave similar results – $\Gamma = 1.81 \pm 0.02$ and $F_{2-10\,\mathrm{keV}} = 1.4 \times 10^{-11}\,\mathrm{erg\,cm^{-2}\,s^{-1}}$ (*ASCA*) vs. $\Gamma = 1.86 \pm 0.02$ and $F_{2-10\,\mathrm{keV}} = 1.2 \times 10^{-11}\,\mathrm{erg\,cm^{-2}\,s^{-1}}$ (*XMM-Newton*; see Table 1).

The UV analyses for the auxiliary objects are presented in Eracleous et al. (2006, in preparation, including the computation of α_{ox}), Ho et al. (1996), Barth et al. (1998), and Barth et al. (1996). The 3C 332 monochromatic flux, measured at 3700 Å, was ∼40% brighter during the SDSS observation than the earlier HST observation. Since Eracleous et al. have a direct 2500 Å measurement, we use it instead of the value inferred by extrapolating the SDSS spectrum. We note that the auxiliary sample of double-peaked emitters is not representative of the SDSS sample of double-peaked emitters – they are all RL, at low redshift, and predominantly low optical/UV luminosity sources.

3. X-RAY PROPERTIES OF THE DOUBLE-PEAKED SAMPLE

The presence of X-ray limits (three main-sample double-peaked emitters and 40 Steffen et al. 2006 RQ AGN) in optically selected samples requires the use of proper statistical tools when making sample comparisons. In this section we use the Astronomy SURVival Analysis package, ASURV (LaValley, Isobe, & Feigelson 1992; Isobe et al. 1986), to calculate sample means using the Kaplan-Meier (K-M) estimator, as well as a set of nonparametric sample-comparison tests for censored data — the logrank test, Gehan generalized Wilcoxon test, and Peto & Prentice generalized Wilcoxon test (e.g.,

TABLE 4
Auxiliary Sample

Object (1)	z (2)	Γ (3)	L(0.1–2.4 keV) (4)	L(2–10 keV) (5)	$f_{2500\,\text{Å}}$ (6)	$\alpha_{\rm ox}$ (7)	$l_{2500\,\text{Å}}$ (8)	Observatory (9)	Reference (10)	Class (11)
NGC 1097	0.0043	1.64±0.03	0.041	0.00668	0.150	−1.22	25.763	*Chandra*	1	LINER
Pictor A	0.0350	1.80±0.03	96	36.0	0.340	−0.80	27.960	*ASCA*	1	BLRG
B2 0742+31	0.4610	1.80 fixed	3200	...	0.640	−1.30	30.688	*ROSAT*	1	RL quasar
PKS 0921−213	0.0531	1.74±0.03	54	42.5	0.370	−1.04	28.370	*XMM*	1	BLRG
M 81	0.00086	1.89±0.01	0.039	0.0175	0.310	−0.91	24.686	*XMM*	2,3	LINER
NGC 4203	0.00362	1.85±0.10	0.0190	0.0330	0.036	−1.02	24.993	*Chandra*,*ASCA*	3,4,5	LINER
NGC 4579	0.00507	1.82±0.03	0.26	0.20	0.059	−0.82	25.502	*XMM*	3,6	LINER
Arp 102B	0.0244	1.58±0.03	2.8	15.7	0.100	−1.02	27.108	*ASCA*	1	BLRG
PKS 1739+184	0.1859	1.80±0.03	550	...	0.790	−1.25	29.867	*ROSAT*	1	RL quasar
3C 390.3	0.0555	1.75±0.03	150	139.	0.330	−0.87	28.361	*ASCA*	1	BLRG

Note. — (1) Object name; (2) Redshift; (3) 2–10 keV power-law slope; (4) 0.1–2.4 keV luminosity in units of $10^{42}\,\text{erg}\,\text{s}^{-1}$; (5) 2–10 keV luminosity in units of $10^{42}\,\text{erg}\,\text{s}^{-1}$; (6) the 2500 Å monochromatic flux in mJy; (7) the UV-to-X-ray index, $\alpha_{\rm ox}$; (8) the logarithm of the 2500 Å monochromatic luminosity in units of $\text{erg}\,\text{s}^{-1}\,\text{Hz}^{-1}$; (10) References: 1) Eracleous et al. sample. 2) Ho et al. (1996) UV spectrum of M 81 3) this work; we used the ObsID 397 *Chandra* observation to obtain the fluxes and flux ratios (columns 4, 5, and 7) of NGC 4203 (see also Ho et al. 2001), the ObsID 0111800101 *XMM-Newton* observation for M 81 (see also Page et al. 2004b), and the ObsID 0112840101 *XMM-Newton* observation for NGC 4579 (see also Terashima et al. 1998, 2000; Eracleous et al. 2002) 4) Barth et al. (1998) UV spectrum of NGC 4203 5) Iyomoto et al. (1998) 2–10 keV spectral index of NGC 4203. 6) NGC 4579 UV spectrum from Barth et al. (1996); (11) Optical/radio classification.

§ III of Feigelson & Nelson 1985 and references therein). All three tests give better results if the sample sizes are similar and the censoring distributions are equal. The Peto & Prentice test is less vulnerable to different censoring distributions than the logrank or Gehan tests (see the discussion in § 5b of Feigelson & Nelson 1985; Latta 1981). Fleming et al. (1980) develop a modified Smirnov test for censored datasets, as the logrank and Gehan tests are insensitive in the case of "crossing-hazards alternatives" (i.e., if the K-M estimator distribution functions of the different samples are not close to parallel but cross over instead); this is relevant when comparing the RL double-peaked emitters with the Steffen et al. (2006) sample discussed below.

3.1. *X-ray Properties of the Double-Peaked Emitters Observed by* ROSAT

To estimate the UV-to-X-ray spectral index, $\alpha_{\rm ox} = -0.3838\log[F_\nu(2500\,\text{Å})/F_\nu(2\,\text{keV})]$, we need a measure of the monochromatic flux at rest-frame 2 keV. The majority (22) of the objects in our sample have been observed only in the soft X-ray band (0.1–2.4 keV), and their spectra have insufficient counts to study their spectral shapes in detail. We first obtain 0.5–2 keV counts and fluxes, and 2 keV monochromatic fluxes (assuming a power-law model with $\Gamma = 2$, modified by Galactic absorption for all sources) following the procedure described in Strateva et al. (2005) and used by Steffen et al. (2006); we list the results in Table 1. The use of a uniform power-law model to determine the rest-frame 2 keV monochromatic luminosity and $\alpha_{\rm ox}$ is necessary for the purpose of comparison with the Strateva et al. (2005) and Steffen et al. (2006) sources. It is also preferable because of the large uncertainties of the hardness-ratio-estimated photon indices (which are also inadequately constrained for 9 of the 22 ROSAT double-peaked emitters and potentially affected by intrinsic absorption as discussed below).

In addition to the above analysis, we also estimate the spectral shape of the *ROSAT*-observed main-sample AGN using the standard hardness ratio, HR1, defined as HR1 = $(B - A)/(B + A)$, where A and B represent the total numbers of photons in the 0.11–0.41 keV and 0.5–2 keV bands, respectively. Assuming no intrinsic absorption above the Galactic value, and spectra well represented by a power-law models, we can derive a one-to-one relationship between the power-law photon index Γ and HR1. We used PIMMS[6] to create a grid of expected HR1 values assuming an absorbed power-law model with different input photon indices and absorbing Galactic column densities spanning the observed range ($10^{20}\,\text{cm}^{-2} < N_H < 5\times10^{20}\,\text{cm}^{-2}$). We found cubic polynomial relations between Γ and HR1 for each absorbing column and used these to estimate the photon index associated with each observed HR1, N_H pair. To estimate the photon-index uncertainties, we propagated uncertainties of the count rates in the 0.5–2 keV and 0.11–0.41 keV *ROSAT* bands using the method described in §1.7.3 of Lyons (1991). The results are given in Table 1. The three double-peaked emitters, which are undetected in the 0.5–2 keV band, have no HR1 photon index estimates. Six of the remaining 19 double-peaked emitters detected by *ROSAT* were detected in the 0.5–2 keV band only; for these we can estimate only an HR1 lower limit and a corresponding upper limit on the power-law slope Γ. Any intrinsic absorption in excess of Galactic will translate into an underestimate of the true value of Γ. This fact is of particular significance for the six double-peaked emitters without 0.11–0.41 keV detections, since the upper-limit values of Γ reported in Table 1 could be underestimated, rendering them useless for comparison. In § 3.4 we point out that this could indeed be the case for a fraction of the AGN in the current sample.

3.2. *X-ray Properties of the Double-Peaked Emitters Observed by* XMM-Newton *and* Chandra

For the seven main-sample double-peaked emitters with hard-band coverage we were able to measure the monochromatic flux at 2 keV (rest-frame) directly from the spectrum and report the corresponding 2 keV monochromatic luminosities, together with their UV-to-X-ray indices in Table 1. These 2 keV measurements might be underestimates of the true values if intrinsic ab-

[6] http://heasarc.gsfc.nasa.gov/docs/software/tools/pimms.html

TABLE 5
X-ray Properties of the *ROSAT* Subsample

Object (1)	z (2)	Count Rate (3)	Counts (4)	N_H (5)	F(0.5–2 keV) (6)	$l_{2\mathrm{keV}}$ (7)	$l_{2500\,\text{Å}}$ (8)	α_{ox} (9)	Γ (10)	R (11)
022417.17−092549.3	0.3120	0.02240	232	2.91	2.78	26.10	29.45	−1.29	$2.6^{+0.1}_{-0.1}$	<0.7
081329.29+483427.9	0.2740	0.03080	133	4.58	4.03	26.13	29.29	−1.21	$2.0^{+0.4}_{-0.4}$	<0.6
092108.63+453857.4	0.1740	0.09070	379	1.51	10.79	26.11	28.45	−0.90	$1.0^{+0.1}_{-0.1}$	4.0
092813.25+052622.5	0.1870	0.01460	38	3.76	1.86	25.42	28.57	−1.21	$<2.8^{+0.3}_{-0.7}$	<0.6
094215.13+090015.8	0.2130	0.01120	11	3.10	1.40	25.42	29.36	−1.51	$<2.3^{+0.3}_{-0.4}$	<0.4
094745.15+072520.6	0.0860	0.01420	152	3.01	1.77	24.66	28.39	−1.43	$1.6^{+0.2}_{-0.2}$	3.2
095427.61+485638.1	0.2480	0.01200	26	0.98	1.40	25.57	28.97	−1.30	$1.6^{+0.5}_{-0.5}$	<0.9
095802.84+490311.1	0.2420	0.01580	20	0.94	1.33	25.67	29.04	−1.29	$2.5^{+0.3}_{-0.7}$	<0.7
104132.78−005057.5	0.3030	0.03340	142	4.44	4.34	26.26	29.29	−1.16	$2.4^{+0.4}_{-0.4}$	<0.6
110109.58+512207.1	0.2520	0.01010	12	1.09	1.19	25.52	29.17	−1.40	$<1.5^{+0.3}_{-0.4}$	<0.9
114454.86+560238.2	0.2310	0.01610	47	1.10	1.89	25.63	28.79	−1.21	$2.5^{+0.2}_{-0.3}$	<0.7
114719.22+003351.2	0.2620	0.00420	<16	2.28	<0.51	<25.19	29.16	<−1.52	...	<1.1
115038.86+020854.2	0.1090	0.00870	44	2.17	1.06	24.67	27.59	−1.12	$<1.6^{+0.3}_{-0.3}$	<0.7
115741.94−032106.1	0.2200	0.00440	<11	2.32	<0.54	<25.03	29.06	<−1.54	...	<0.6
120848.82+101342.6	0.1160	0.05370	86	1.67	6.43	25.50	27.94	−0.94	$2.3^{+0.1}_{-0.1}$	<0.4
130723.13+532318.9	0.3230	0.02700	241	1.46	3.21	26.20	29.40	−1.23	$2.1^{+0.1}_{-0.1}$	<1.0
132355.69+652233.0	0.2260	0.00330	16	2.01	0.39	24.93	28.65	−1.43	$<2.4^{+0.3}_{-0.4}$	<1.1
144302.76+520137.2	0.1410	0.12040	787	1.63	14.38	26.04	28.44	−0.92	$1.7^{+0.1}_{-0.1}$	3.6
161742.53+322234.3	0.1510	0.00870	84	2.02	1.05	24.96	28.96	−1.53	$<1.2^{+0.3}_{-0.3}$	3.3
164031.86+373437.2	0.2800	0.02010	60	1.32	2.38	25.92	28.74	−1.08	$2.3^{+0.2}_{-0.2}$	<1.1
170102.29+340400.6	0.0950	0.03100	140	2.06	3.75	25.08	28.24	−1.21	$1.9^{+0.1}_{-0.1}$	<0.3
213338.42+101923.6	0.1260	0.00420	<16	4.83	<0.55	<24.51	28.36	<−1.48	...	<0.9

Note. — (1) the SDSS name given in the J2000 epoch RA and Dec form, HHMMSS.ss±DDMMSS.s; (2) redshift; (3) PSPC 0.5–2 keV count rate, in counts per second; (4) total counts in the 0.5–2 keV band; (5) Galactic absorbing column, in units of $10^{20}\,\mathrm{cm}^{-2}$; (6) flux in the 0.5–2 keV band (assuming a power-law spectrum with $\Gamma = 2$), corrected for Galactic absorption, in units of $10^{-13}\,\mathrm{erg\,cm^{-2}\,s^{-1}}$; (7) the logarithm of the 2 keV monochromatic luminosity in units of $\mathrm{erg\,s^{-1}\,Hz^{-1}}$; (8) the logarithm of the 2500 Å monochromatic luminosity in units of $\mathrm{erg\,s^{-1}\,Hz^{-1}}$; (9) the UV-to-X-ray spectral index, α_{ox}; (10) the hardness-ratio estimate of the spectral slope, Γ; (11) R is the radio-loudness indicator, $R = \log(F_{1.4\,\mathrm{GHz}}/F_i)$, where F_i is the SDSS i-band flux and $R \geq 1$ is considered radio loud.

sorption above $10^{22}\,\mathrm{cm}^{-2}$ (assuming $z \approx 0.2$) is present. In the analysis of individual objects below, we show that this is probably the case for only two of the *XMM-Newton* or *Chandra* observed objects and we correct the 2 keV measurements accordingly.

Five of the double-peaked emitters have sufficient counts to obtain absorbed power-law fits using XSPEC.[7] For the remaining two objects we attempt to constrain the intrinsic absorption assuming a standard power-law photon index. In all cases we include the Galactic absorption in the model fits. The results of the analysis for all seven double-peaked emitters with hard-band X-ray detections are presented below.

3.2.1. *SDSSJ 0043+0051 (UM 269)*

SDSSJ 0043+0051 ($z = 0.3081$) has been observed by *XMM-Newton*, *ASCA*, and *ROSAT* (see Table 1). The *XMM-Newton* spectral fits were published by Page et al. (2004a); we confirm their results: the observed 2–10 keV spectrum can be represented by a power law with photon index $\Gamma = 1.70 \pm 0.06$ and Galactic absorption ($\chi^2/DoF = 0.9$ for 79 DoF, EPIC pn fit). The 0.5–10 keV spectrum and fit are shown in Figure 6. When this model is extended to lower energies, a soft-excess is detected. There is no evidence of Fe Kα emission; for a line centered at 6.4 keV with a width of 10 eV, we obtain an upper limit of 180 eV for the equivalent width (EW) at 90% confidence (Page et al. 2004 estimate EW< 80 keV at 90% confidence). For comparison, an *ASCA* power-law fit for a 31 ks observation obtained five years earlier (as reported in the Tartarus database at HEASARC[8]) has $\Gamma = 1.4 \pm 0.1$, a 60% higher flux in the 2–10 keV band, $F_{2\text{–}10\,\mathrm{keV}} = 1.6 \times 10^{-12}\,\mathrm{erg\,cm^{-2}\,s^{-1}}$, and no evidence for Fe Kα emission.

3.2.2. *SDSSJ 0057+1446*

The observed *Chandra* ACIS-S count rate per frame for SDSSJ 0057+1446 ($z = 0.1722$) is ~ 0.57 counts s^{-1} (with frame-time of 0.441 s) and is high enough for photon pile-up to be important even for an off-axis angle of 3.3′. Pile-up is the incidence of two or more X-ray photons in one (or more) neighboring CCD pixels within one frame time. The CCD electronics may falsely regard these events as a single event with an amplitude given by the sum of the electron charge, resulting in a decrease of the apparent count rate of the source, an artificial hardening of its spectrum, and the apparent distortion of the point-spread function (PSF) of point-like objects. It can also alter the photon event grades and lead to a loss of events when standard grade filtering is applied to the data.

To account for the effects of pile-up, we initially analyzed spectra of SDSSJ 0057+1446 from annuli of var-

[7] http://heasarc.gsfc.nasa.gov/docs/xanadu/xspec/

[8] High Energy Astrophysics Science Archive Research Center, http://heasarc.gsfc.nasa.gov/

TABLE 6
X-ray Properties of the *XMM-Newton*/*Chandra* Subsample

Object (1)	z (2)	$l_{2500\,\text{Å}}$ (3)	$l_{2\,\text{keV}}$ (4)	$\alpha_{\rm ox}$ (5)	F(2–10 keV) (6)	Γ (7)	Fit Range (8)	Model (9)	N_H (10)	$N_{H,\rm intr}$ (11)	Counts (12)	R (13)
0043+0051	0.3081	29.76	26.53	−1.24	9.3	1.70±0.06	2–10	PL	2.31	...	1704	0.8
0057+1446	0.1722	30.03	26.55	−1.33	38.0	2.2±0.4	1–10	PL	4.37	...	403	<0.0
0918+5139	0.1854	29.18	25.33	−1.48	2.9	1.4±0.3	0.4–11	PAPL	1.45	500 ± 100	243	<0.3
...	0.1854	29.18	25.05	−1.58	2.0	1.3±0.4	0.3–11	APL	1.45	130 ± 60	145	<0.3
0938+0057	0.1704	28.95	25.95	−1.15	18.2	1.5 fixed	0.3–11	APL	4.22	200 ± 40	132	<−0.3
1111+4820	0.2809	29.49	25.73	−1.44	2.6	1.7±0.2	2–10	PL	1.24	...	295	1.7
1134+4912	0.1765	28.57	24.46	−1.58	>0.25	1.9 fixed	0.2–10	PL	1.55	...	24	0.8
2304−0841	0.0469	28.59	26.19	−0.92	302.	1.71±0.02	2–10	PLG	3.60	...	27200	1.0

Note. — (1) the SDSS name given in the J2000 epoch RA and Dec form, HHMMSS.ss±DDMMSS.s; (2) redshift; (3) the logarithm of the rest-frame 2500 Å monochromatic luminosity in units of $\rm erg\,s^{-1}\,Hz^{-1}$; (4) the logarithm of the rest-frame 2 keV monochromatic luminosity in units of $\rm erg\,s^{-1}\,Hz^{-1}$; (5) the UV-to-X-ray spectral index, $\alpha_{\rm ox}$; (6) the unabsorbed flux in the observed 2–10 keV band in units of $10^{-13}\,\rm erg\,cm^{-2}\,s^{-1}$; (7) the spectral photon index, Γ; (8) the range of the spectral fit, in keV; (9) spectral-fit models: PL corresponds to a simple power-law model including Galactic absorption (i.e. "wabs pow" in XSPEC); APL refers to a intrinsically absorbed power-law model ("wabs zwabs pow)" in XSPEC), with the column density of the intrinsic absorption given in column (11); PAPL refers to a partially absorbed power-law model ("wabs zpcfabs pow)" in XSPEC); PLG refers to a power-law model with galactic absorption and a Gaussian Fe-Kα line ("wabs pow zgaus" in XSPEC); (10) The Galactic absorption at the AGN position in units of $10^{20}\,\rm cm^{-2}$; (11) any intrinsic absorption in units of $10^{20}\,\rm cm^{-2}$; (12) the total counts (*Chandra* ACIS-S or *XMM-Newton* pn, except for SDSSJ 1134+4912, where the *XMM-Newton* MOS counts are given) in the energy range given in column (8); (13) the radio loudness, $R = \log(F_{1.4GHz}/F_i)$.

ious inner radii — 0″, 4″, 1.0″, 1.5″ , and 2″ — and an outer radius of 3.4″, excluding events from the core of the PSF in annuli #2 through #5, which are most affected by pile-up. The effective-area files used when modeling the annular spectra were corrected for the energy dependence of the *Chandra* PSF. We fit the annular spectra with simple power-law models modified by Galactic absorption. The resulting 1–10 keV spectral slopes are $\Gamma = 1.86 \pm 0.08$ (annulus #1), $\Gamma = 1.9 \pm 0.1$ (#2), $\Gamma = 2.0 \pm 0.2$ (#3), and $\Gamma = 2.2 \pm 0.4$ (#4), with no need for absorption above Galactic. The last annulus (#5) has very few photons resulting in a poorly constrained spectral index, $\Gamma = 2 \pm 1$. Based on the spectral fit in annulus #4 (1.5–3.4″) which is shown in Figure 6, we estimate the pile-up corrected $\Gamma = 2.2 \pm 0.4$. To estimate the fraction of events lost due to pile-up we used the forward spectral-fitting tool LYNX that simulates pile-up (Chartas et al. 2000). LYNX simulates the propagation of individual photons through the *Chandra* mirrors and ACIS, and it takes into account the possible overlap of events within one frame time. We find that the pile-up fraction is ∼ 20% in the 0.5–2 keV band (the pile-up corrected flux is $3.1 \times 10^{-12}\,\rm erg\,cm^{-2}\,s^{-1}$) and is negligible in the 2–10 keV band ($F_{2-10\,\rm keV} = 3.8 \times 10^{-12}\,\rm erg\,cm^{-2}\,s^{-1}$).

3.2.3. *SDSSJ 0918+5139*

SDSSJ 0918+5139 ($z = 0.1854$) was serendipitously observed by both *Chandra* and *XMM-Newton* (see Table 1) as a result of its proximity (∼6 arcmin) to a nearby cluster, Abell 773 ($z = 0.21$). The *XMM-Newton* pn spectrum has 243 counts in the 2–11 keV band. A power-law fit with no intrinsic absorption above the Galactic value provides a marginally acceptable fit in the 2–11 keV band – $\chi^2/DoF \approx 1.5$ for $15\,DoF$ with $\Gamma = 0.6 \pm 0.2$. The 2–11 keV fit can be improved by adding intrinsic absorption – $\chi^2/DoF \approx 1.1$ for $14\,DoF$, with $\Gamma = 1.7 \pm 0.5$ and $N_{\rm H,intr} = (8 \pm 4) \times 10^{22}\,\rm cm^{-2}$, but neither of these fits is acceptable over the full 0.4–11 keV *XMM-Newton* band (the best fit has $\chi^2/DoF \approx 1.7$, $21\,DoF$). A model with a partial absorber in addition to the Galactic one – $\Gamma = 1.4 \pm 0.3$, $N_{\rm H,intr} = (5 \pm 1) \times 10^{22}\,\rm cm^{-2}$, and a covering fraction of $f_{\rm c} = 0.92 \pm 0.05$ – provides an acceptable fit in the 0.4–11 keV band: $\chi^2/DoF \approx 1.0$ for $20\,DoF$. The *Chandra* spectrum has only 102 counts in the 2–10 keV region and can be represented by a $\Gamma = 1.5 \pm 0.4$ power law fit with no intrinsic absorption above the Galactic value ($\chi^2/DoF \approx 1.1$, $17\,DoF$). The full *Chandra* band (0.3–11 keV, 145 counts) requires an intrinsic absorber ($\chi^2/DoF \approx 1.5$ vs. $\chi^2/DoF \approx 1.1$, $24\,DoF$) $N_{\rm H,intr} = (1.3 \pm 0.6) \times 10^{22}\,\rm cm^{-2}$ and has a slightly flatter spectral slope, $\Gamma = 1.3 \pm 0.4$. The data suggests that the intrinsic absorber has changed in the seven months separating the *XMM-Newton* and *Chandra* observations. In the following sections (§ 3.3 and § 3.4) we use the 0.4–11 keV *XMM-Newton* results, which were obtained 4.6 months after the optical spectrum, have better signal-to-noise, and more accurate fit parameters.

The absorption corrected 2–10 keV fluxes are consistent between the two observations within the (90% confidence) errorbars: $F_{2-10\,\rm keV} = 2.0^{+0.7}_{-0.4} \times 10^{-13}\,\rm erg\,cm^{-2}\,s^{-1}$ (*Chandra*), and $F_{2-10\,\rm keV} = 2.9^{+0.8}_{-1.2} \times 10^{-13}\,\rm erg\,cm^{-2}\,s^{-1}$ (*XMM-Newton* pn). In the soft band, the observed fluxes are $F_{0.5-2\,\rm keV} = 1.8^{+0.7}_{-1.5} \times 10^{-14}\,\rm erg\,cm^{-2}\,s^{-1}$ (*Chandra*) and $F_{0.5-2\,\rm keV} = 0.9^{+0.4}_{-0.7} \times 10^{-14}\,\rm erg\,cm^{-2}\,s^{-1}$ (*XMM-Newton* pn); the intrinsic absorption correction could increase those by a factor of 3 (*Chandra*) to 6 (*XMM-Newton*).

3.2.4. *SDSSJ 0938+0057*

SDSSJ 0938+0057 ($z = 0.1704$) has a 132 count detection (0.3–10 keV) in a 1.3 ks *Chandra* observation. The spectrum is hard, implying high intrinsic obscuration and/or a flat power-law. If we fix the absorbing column to the Galactic value, $N_H = 4.2 \times 10^{20}\,\rm cm^{-2}$, a simple power-law fit in the 2–10 keV band (87 counts) returns $\Gamma = 0.9 \pm 0.4$. Alternatively, assuming a standard power-law slope, $\Gamma = 1.9$ for RQ AGN, we infer an intrinsic absorbing column of $N_{\rm H,intr} = (6.4 \pm 2.3) \times 10^{22}\,\rm cm^{-2}$. Neither of these fits is applicable over the full 0.3–10 keV range: the required photon index drops to $\Gamma = 0.1 \pm 0.1$ if we assume no intrinsic absorption, which is unrealistic considering the uniformity of the power-law slopes measured in RQ AGN (1.9 ± 0.5, see, for example, Figure 6 of Vignali et al. 2005, and references therein), and the best $\Gamma = 1.9$ model including intrinsic absorption is in-

adequate ($\chi^2/DoF \approx 1.6$, $24\,DoF$). The full 0.3–10 keV band spectrum can be represented by an intrinsically absorbed model with fixed $\Gamma = 1.5$ and an intrinsic absorbing column of $N_{\rm H,intr} = (2.0 \pm 0.4) \times 10^{22}\,{\rm cm}^{-2}$ ($\chi^2/DoF \approx 1.3$, $24\,DoF$). For a simple intrinsically absorbed power law model, photon indices steeper than $\Gamma = 1.5$ are excluded. If we allow an intrinsic absorber with partial coverage, the intrinsic absorbing column increases $N_{\rm H,intr} = (5 \pm 1) \times 10^{22}\,{\rm cm}^{-2}$, allowing a $\Gamma = 1.8$ fit ($\chi^2/DoF \approx 1.1$, $24\,DoF$). Higher signal-to-noise data is necessary to distinguish between the flat photon index, intrinsically absorbed model, and the steep photon index, partially absorbed model.

We adopt the simpler 0.3–10 keV band $\Gamma = 1.5$ model fit (see Table 1 and Figure 6) and estimate the unabsorbed fluxes in the hard and soft bands: $F_{2\text{–}10\,{\rm keV}} = 1.3^{+0.3}_{-0.7} \times 10^{-12}\,{\rm erg\,cm^{-2}\,s^{-1}}$ and $F_{0.5\text{–}2\,{\rm keV}} = 1.2^{+0.2}_{-0.4} \times 10^{-12}\,{\rm erg\,cm^{-2}\,s^{-1}}$.

3.2.5. *SDSSJ 1111+4820*

SDSSJ 1111+4820 ($z = 0.2809$) falls within the field of view of two *XMM-Newton* observations, one of which (Obs. ID 0059750401) is heavily affected by background flaring. We used the pn observation from June 2002 (Obs. ID 0104861001), which has a much longer effective exposure time, to extract and fit the 2–10 keV spectrum of SDSSJ 1111+4820. The results are given in Figure 6 and in Table 1. The 2–10 keV spectrum is well fit by a simple power law with Galactic absorption with $\Gamma = 1.7 \pm 0.2$. If we extend this model to lower energies, the negative residuals below 2 keV could indicate the presence of intrinsic absorption. Excess intrinsic absorption, however, is not required by the data: the 0.5–10 keV spectrum also admits a power-law fit with a flatter photon index – $\Gamma = 1.35 \pm 0.07$ – and no intrinsic absorption ($\chi^2/{\rm DoF} = 1.2$ for $48\,DoF$).

3.2.6. *SDSSJ 1134+4912*

SDSSJ 1134+4912 ($z = 0.1765$) is situated less than $10''$ from another, optically fainter, point-like object in the SDSS image (SDSS J113451.64+491200.8, with an r-band magnitude of 21.8). Both this fainter object and the double-peaked emitter of interest to us are detected separately in the *XMM-Newton* MOS images with similar counts; the larger pixel size of the pn ($4.1''$ for pn vs. $1.1''$ for the MOS detectors) blends the two objects, with a centroid closer to the fainter MOS object. The *ROSAT* PSPC (PSF FWHM of $\sim 25''$ at 1 keV and an observed off-axis angle of $\sim 9'$) or HRI (with a 50% power radius of $\sim 9''$ for an off-axis angle of $\sim 12'$) lack the angular resolution to separate the two objects clearly and will not be considered here. The measured 0.5–2 keV flux of the double-peaked emitter is $F_{0.5\text{–}2\,{\rm keV}} = (2 \pm 1) \times 10^{-14}\,{\rm erg\,cm^{-2}\,s^{-1}}$ for a $6''$ aperture (MOS2). Using the EPIC MOS on-axis PSF (which does not change much for objects at an off-axis angle of $7'$ for energies <2 keV), we estimate that the total flux of SDSSJ 1134+4912 is $F_{0.5\text{–}2\,{\rm keV}} \approx 3 \times 10^{-14}\,{\rm erg\,cm^{-2}\,s^{-1}}$. On account of the proximity to the second source, the small aperture used for the flux estimate, and the small number of total counts, the X-ray flux and 2 keV monochromatic luminosity of this object are uncertain. Using the Cash statistic, we can obtain an acceptable fit to the MOS spectrum using a power-law model with $\Gamma = 1.9$ and an absorbing column density equal to the Galactic value. The high resolution of *Chandra* is necessary to measure the X-ray properties of this object properly.

3.2.7. *SDSSJ 2304−0841 (MCG-2-58-22, Mrk 926)*

SDSSJ 2304−0841 is a nearby ($z = 0.0469$) Seyfert galaxy that has been observed repeatedly with most current and past X-ray observatories (see Appendix A). Figure 6 shows the spectrum in the 0.5–220 keV range, originally published by Bianchi et al. (2004), overlaid with a model consisting of an exponentially cutoff power-law, reflection from an isotropically illuminated cold slab (Magdziarz & Zdziarski 1995), and a Gaussian Fe Kα line. Our 2–220 keV XSPEC fits confirm their results: the spectrum above 2 keV is well represented by an absorbed and Compton reflected power law with $\Gamma = 1.76 \pm 0.04$, absorption equal to the Galactic column density, a 6.4 keV Fe Kα line with $EW = 60^{+80}_{-40}$ keV and energy dispersion $\sigma = (120 \pm 80)$ eV (corresponding to FWHM$\approx 13000\,{\rm km\,s^{-1}}$, comparable to that of the Hα line, FWHM$\approx 11400\,{\rm km\,s^{-1}}$), and a soft excess below 2 keV. If we consider only the 2–10 keV region (see Table 1), the power law fit with no intrinsic absorption and a Gaussian Fe Kα line has $\Gamma = 1.71 \pm 0.02$, consistent with the value obtained above in the 0.5–220 keV range. Three previous spectra observed with *ASCA* obtained in 1993 and 1997 (Weaver et al. 1995, 2001) show similar spectral shapes, with $1.71 < \Gamma < 1.84$ and evidence for some intrinsic absorption ($N_{\rm H,intr} \approx 10^{21}\,{\rm cm}^{-2}$) in the two 1997 spectra. Judging from the relation between X-ray and optical variability, which is detailed in Appendix A, the presence of intrinsic absorption seems unrelated to the shape of the Hα line. Both the 1993 and one of the 1997 spectra show clear Fe Kα lines, whose parameters depend on the continuum model (Weaver et al. 1995, 2001); the presence of a strong Fe Kα line also appears unrelated to the single- or double-peaked shape of the optical Balmer lines (Appendix A).

3.3. *UV-to-X-ray Slope*

The rest-frame UV and soft X-ray emission from AGN are correlated, with more luminous AGN emitting relatively less X-rays per unit UV luminosity (e.g., Strateva et al. 2005; Steffen et al. 2006, and references therein). Consequently a proper comparison of the X-ray emission of double-peaked emitters with those of normal AGN should take this relation into account. Figure 7 shows the 2500 Å vs. the 2 keV monochromatic luminosities of the double-peaked emitters in comparison with those of RQ AGN from the Steffen et al. (2006) sample. The Steffen et al. (2006) sample includes 333 optically selected RQ AGN with a high X-ray detection fraction (88%), and no evidence of intrinsic absorption in the UV. Over half of the objects in the sample are SDSS AGN, directly comparable to the double-peaked emitters studied here. The remaining objects allow us to extend the UV luminosity range of the comparison sample at each redshift. The RQ double-peaked emitters appear indistinguishable in Figure 7 from normal AGN with similar UV monochromatic luminosities. The majority of the RL double-peaked emitters show excess 2 keV emission, as is characteristic of all RL AGN (e.g., Worrall et al. 1987).

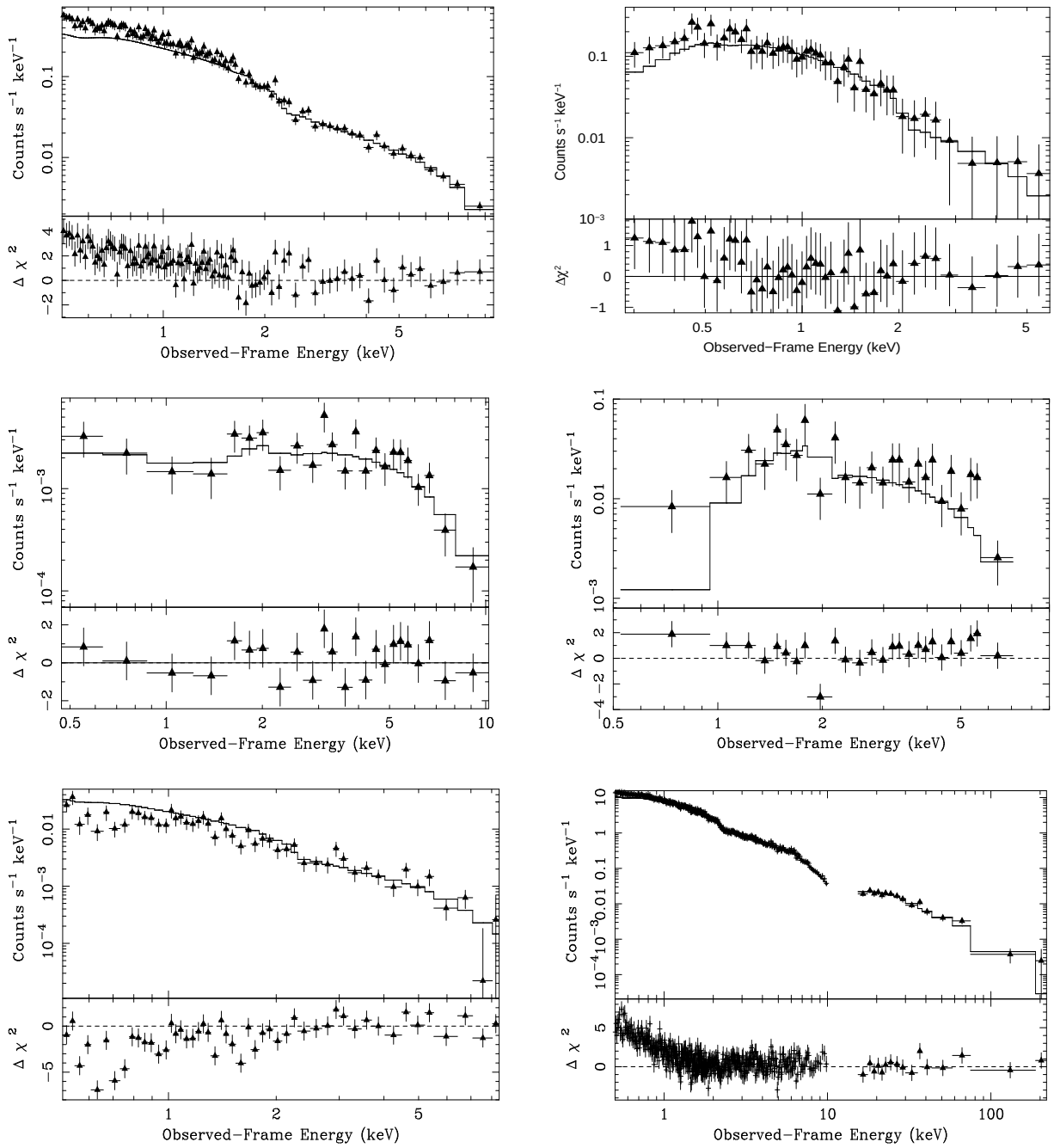

FIG. 6.— X-ray spectra and model fits of five main-sample double-peaked emission AGN: SDSSJ 0043+0051 (*XMM-Newton* pn spectrum, top left), SDSSJ 0057+1446 (*Chandra* spectrum of annulus #4, top right), SDSSJ 0918+5139 (*XMM-Newton* pn spectrum, middle left), SDSSJ 0938+0057 (*Chandra* spectrum, middle right), SDSSJ 1111+4820 (*XMM-Newton* pn spectrum, bottom left), and SDSSJ 2304−0841 (simultaneous *XMM-Newton* and *Beppo-SAX* data, bottom right).

Figure 8 shows the UV-to-X-ray slope, $\alpha_{\rm ox}$, for the double-peaked emitters in comparison with the sample of Steffen et al. (2006). The majority of double-peaked AGN follow the Steffen et al. (2006) $\alpha_{\rm ox}$-$l_{2500\,\text{Å}}$ relation, $\alpha_{\rm ox}(l_{2500\,\text{Å}}) = -0.137 l_{2500\,\text{Å}} + 2.638$, and do not differ substantially from normal AGN with comparable luminosity in the UV. Due to the small range of luminosities probed at each redshift and the strong luminosity-redshift relation in the sample of double-peaked emitters, a partial-correlation analysis for the $\alpha_{\rm ox}$-$l_{2500\,\text{Å}}$ relation (i.e., one that takes into account the $l_{2500\,\text{Å}}$-z relation) is inconclusive. The strength of the $\alpha_{\rm ox}$-$l_{2500\,\text{Å}}$ partial correlation is only 2.3σ with partial Kendall's $\tau_{12,3} = -0.24$, which could indicate either an inability of the partial-correlation analysis to detect a weaker $\alpha_{\rm ox}$-$l_{2500\,\text{Å}}$ anti-correlation on top of a strong $l_{2500\,\text{Å}}$-z correlation ($\tau_{23} = 0.53$), or a genuine lack of an $\alpha_{\rm ox}$-$l_{2500\,\text{Å}}$ relation. Since we know the $l_{2500\,\text{Å}}$-z correlation is very strong for our sample of double-peaked emitters, we believe the former is more likely.

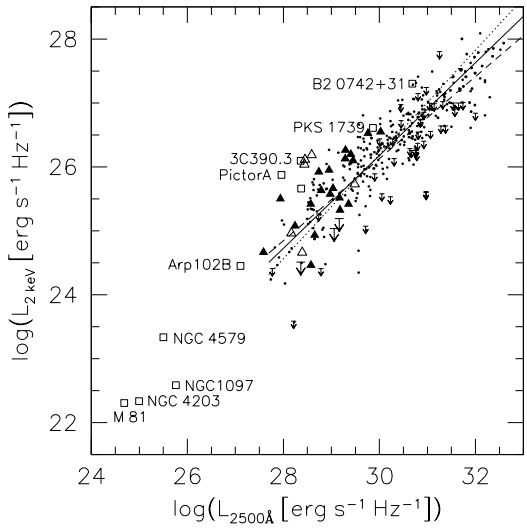

FIG. 7.— Rest-frame UV vs. X-ray monochromatic luminosities of the main SDSS double-peaked sample (open triangles denote RL AGN, solid triangles denote RQ AGN, and large arrows denote X-ray limits), the Steffen et al. (2006) RQ AGN sample (dots and small arrows, indicating X-ray detections and upper limits, respectively), and the auxiliary double-peaked sample (open squares). The solid line is the best-fit bisector linear regression from Steffen et al. (2006); the dashed and dotted lines represent the fits minimizing the residuals in ordinate and the abscissa, respectively (see Steffen et al. 2006 for more details). The difference between the dashed and dotted lines can be used as an indication of the maximum uncertainly in the UV-X-ray relation.

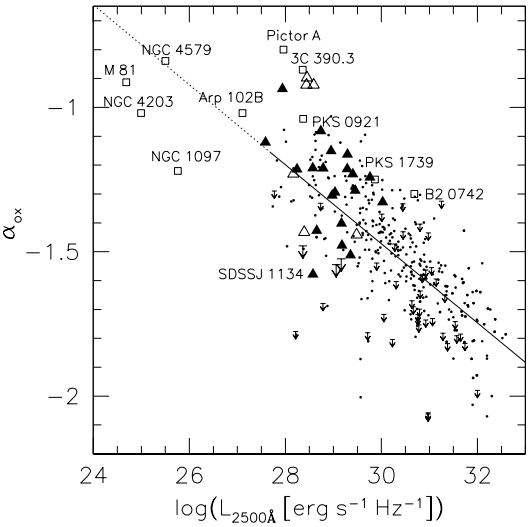

FIG. 8.— Rest-frame UV monochromatic luminosity vs. $\alpha_{\rm ox}$. The symbols are as in Figure 7. The line is the best-fit linear regression from Steffen et al. (2006) with an extrapolation to lower luminosities given by the dotted line.

The top-left panel of Figure 9 presents the histogram of $\alpha_{\rm ox}$ residuals for the RQ main sample of double-peaked emitters, obtained by subtracting the expected $\alpha_{\rm ox}(l_{2500\,\text{Å}})$ from each observed $\alpha_{\rm ox}$, in comparison with that of the full sample and a luminosity-matched subsample ($l_{2500\,\text{Å}} < 30$) from Steffen et al. (2006), shown in the middle left panel of Figure 9. The comparison with the luminosity-matched subsample is useful, as there are some indications that the $\alpha_{\rm ox}$-$l_{2500\,\text{Å}}$ relation might be non-linear (Steffen et al. 2006). The Kaplan-Meier (K-M) estimator mean value of the $\alpha_{\rm ox} - \alpha_{\rm ox}(l_{2500\,\text{Å}})$ residuals for the RQ main sample is $\langle \alpha_{\rm ox} - \alpha_{\rm ox}(l_{2500\,\text{Å}}) \rangle = 0.01 \pm 0.04$, consistent with zero, as is the equivalent K-M estimate, $\langle \alpha_{\rm ox} - \alpha_{\rm ox}(l_{2500\,\text{Å}}) \rangle = -0.02 \pm 0.02$, for the luminosity-matched Steffen et al. (2006) subsample. Both the Gehan and the logrank tests ($T = 1.0$, $P = 32\%$ and $T = 0.4$, $P = 72\%$) confirm that there is no significant difference in the cumulative distributions of the RQ subsample of the main sample and the luminosity-matched Steffen et al. (2006) subsample. The conclusions remain unchanged if we include the full Steffen et al. (2006) sample. Both $\alpha_{\rm ox}$ residual distributions are consistent with being Gaussian, with a width of 0.17 ± 0.04 for the RQ main sample and 0.14 ± 0.01 for the luminosity-matched Steffen et al. (2006) subsample and small positive means (0.07 ± 0.04 and 0.04 ± 0.01, respectively). The specific Gaussian parameters (especially the distribution means) are slightly dependent on the size of the bins used and the fact that we ignore a small number of $\alpha_{\rm ox}$ limits when performing the Gaussian fits, but the fit parameters are generally within the 1σ errors quoted above. In all cases the RQ double-peaked emitters tend to have a broader $\alpha_{\rm ox}$ residual distribution than the corresponding luminosity-matched Steffen et al. (2006) subsample distribution, but the difference is at the 1σ level. If this result is confirmed in larger samples, it could indicate larger X-ray and/or UV variability for the double-peaked emitters. Our current results indicate that the double-peak emitters as a class cannot have dramatically different variability properties than normal active galaxies of similar optical/UV luminosity.

The left panel of Figure 9 shows that RL double-peaked emitters have a significantly different $\alpha_{\rm ox}$ distribution than RQ double-peaked emitters and the Steffen et al. (2006) (full and luminosity-matched) samples. Because of the difference in censoring patterns between the Steffen et al. (2006) sample and the sample of RL double-peaked emitters, the Gehan and logrank tests, which assume no such difference exists, were not used in this comparison. A Peto & Prentice test confirms that the RL double-peaked emitters have $\alpha_{\rm ox}$ residuals which are substantially different from those of normal RQ AGN – $T = 2.3$, $P = 2\%$. The stronger X-ray emission of RL double-peaked emitters in comparison to RQ AGN of similar UV luminosity is also clearly illustrated in Figure 8, where eight of the 11 RL double-peaked emitters with $l_{2500\,\text{Å}} > 27.5$ (where the comparison is strictly possible) have $\alpha_{\rm ox}$ values much flatter than typical RQ AGN. A Peto & Prentice test confirms that the $\alpha_{\rm ox}$ residuals of these 11 RL double-peaked emitters are significantly different than those of the RQ AGN in the Steffen et al. (2006) sample ($T = 4.7$, $P \ll 1\%$). The average $\alpha_{\rm ox}$ residual for these 11 RL double-peaked emitters is 0.21; the median $\alpha_{\rm ox}$ residual is 0.27. Consequently, RL double-peaked emitters are on average $\sim 4\times$ more X-ray luminous than their RQ counterparts, similar to the factor ~ 3 observed for RL AGN as a whole (e.g., Worrall et al. 1987).

It is instructive to compare the positions of the higher and lower luminosity RL double-peaked emitters relative to the extrapolation of the Steffen et al. (2006) relation from Figure 8. The higher luminosity RL objects tend

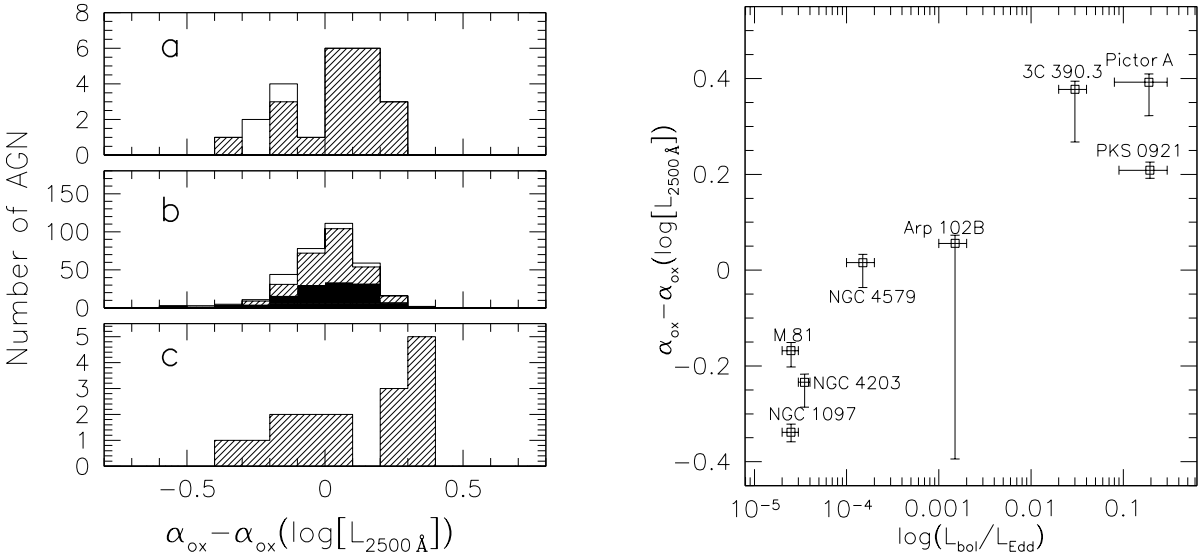

FIG. 9.— *Left:* Comparison between the $\alpha_{ox}-\alpha_{ox}(l_{2500\,Å})$ residual distributions for the RQ AGN from the main sample of double-peaked emitters (panel a, hatched), the Steffen et al. (2006) sample (panel b, hatched), the luminosity-matched subsample of Steffen et al. (2006) (panel b, solid), and the RL double-peaked emitters from both the main and auxiliary samples (panel c, hatched). The open histograms in each panel indicate the $\alpha_{ox}-\alpha_{ox}(l_{2500\,Å})$ limits. *Right:* $\alpha_{ox}-\alpha_{ox}(l_{2500\,Å})$ residuals vs. bolometric luminosity as a fraction of the Eddington luminosity for eight auxiliary sample RL double-peaked emitters. This plot includes objects whose black hole masses were obtained from stellar velocity dispersion measurements.

to have flatter α_{ox} values than expected for RQ objects with similar luminosities, while the LINER galaxies appear to have steeper α_{ox} values. This difference causes the apparently bimodal α_{ox}-residual distribution for RL double-peaked emitters shown in in the bottom-left panel of Figure 9. Lewis & Eracleous (2006) have obtained accurate black-hole mass measurements and estimated the bolometric luminosities of eight of the RL double-peaked emitters included in our study. The right panel of Figure 9 shows the α_{ox} residuals vs. the bolometric luminosities of these eight sources as a fraction of the Eddington luminosity. The error bars in the α_{ox} residuals include the uncertainty due to the intrinsic UV absorption correction and a constant 10% error in both the 2500 Å and 2 keV monochromatic-luminosity measurements. It ignores the possibly large but unknown uncertainties due to the non-simultaneity of the UV and X-ray observations. To estimate the uncertainty due to an intrinsic UV absorption correction from the inferred X-ray absorption (or its upper limit) we assume the Seaton (1979) extinction law and a Galactic N_H/A_V ratio. The uncertainties due to the UV absorption corrections are typically less than a factor of 3, except for Arp 102B, where it is a factor of 20. The correlation between $\alpha_{ox}-\alpha_{ox}(l_{2500\,Å})$ and L/L_{Edd} is strong (partial Kendall's $\tau_{12,3}=0.71$ or $\tau_{12,3}=0.60$) but significant only at the $3.0\,\sigma$ or $3.2\,\sigma$ level when controlling for the dependence of both variables on luminosity or redshift. This observation is consistent with our expectation of a different SED for AGN with low-radiative-efficiency accretion modes in comparison to the standard thin-disk and corona models attributed to higher radiative-efficiency AGN.

Wu & Liu (2004) have used the FWHM and optical monochromatic-luminosity measurements of the S03 and Eracleous & Halpern (1994, 2003) samples to obtain rough estimates of the black-hole masses and accretion rates as a fraction of the Eddington luminosity. Even though the specific measurements of Wu & Liu (2004) are very uncertain (Lewis & Eracleous 2006 find that two of the four black-hole masses in common with their sample were overestimated by an order of magnitude), their general conclusions that double-peaked emitters have diverse accretion rates were confirmed by Lewis & Eracleous (2006). It is therefore encouraging that Wu & Liu (2004) find a similar break (at $L/L_{Edd}\sim 0.001$) in the α_{ox} vs. L/L_{Edd} relation (see their Figure 4) for all known RL double-peaked emitters. Considering the small number of objects (eight with accurate black-hole mass measurements and a total of 26 in Wu & Liu 2004) and the large uncertainties in α_{ox} (caused by both variability and measurement errors) for low-luminosity AGN, as well as the strong third-variable dependences, these findings need confirmation in larger samples.

3.4. *X-ray Spectral Shapes*

Figure 10 shows a comparison between the X-ray spectral slopes measured in the soft (0.1–2 keV, panels a and b) and hard (2–10 keV, panels c and d[9]) bands for the double-peaked emitters with those for similar broad-line AGN which show no evidence of disk emission in the optical. The comparison samples of normal AGN were selected from Laor et al. (1997; $\mathrm{FWHM}_{H\beta}>2000\,\mathrm{km\,s^{-1}}$), Walter & Fink (1993, $\mathrm{FWHM}_{H\beta}>2000\,\mathrm{km\,s^{-1}}$ and $\chi^2/DoF<1.1$), Brinkmann et al. (1997), Piconcelli et al. (2005; $\mathrm{FWHM}_{H\beta}>2000\,\mathrm{km\,s^{-1}}$), the Seyfert 1 galaxies from Nandra et al. (1997), and the BLRG and RL quasars from Sambruna et al. (1999). Only broad-

[9] As indicated in Table 1, the hard-band fitting region was extended for five of the main-sample double-peaked emitters to include the soft band in order to increase the total photon counts to better model the intrinsic absorption.

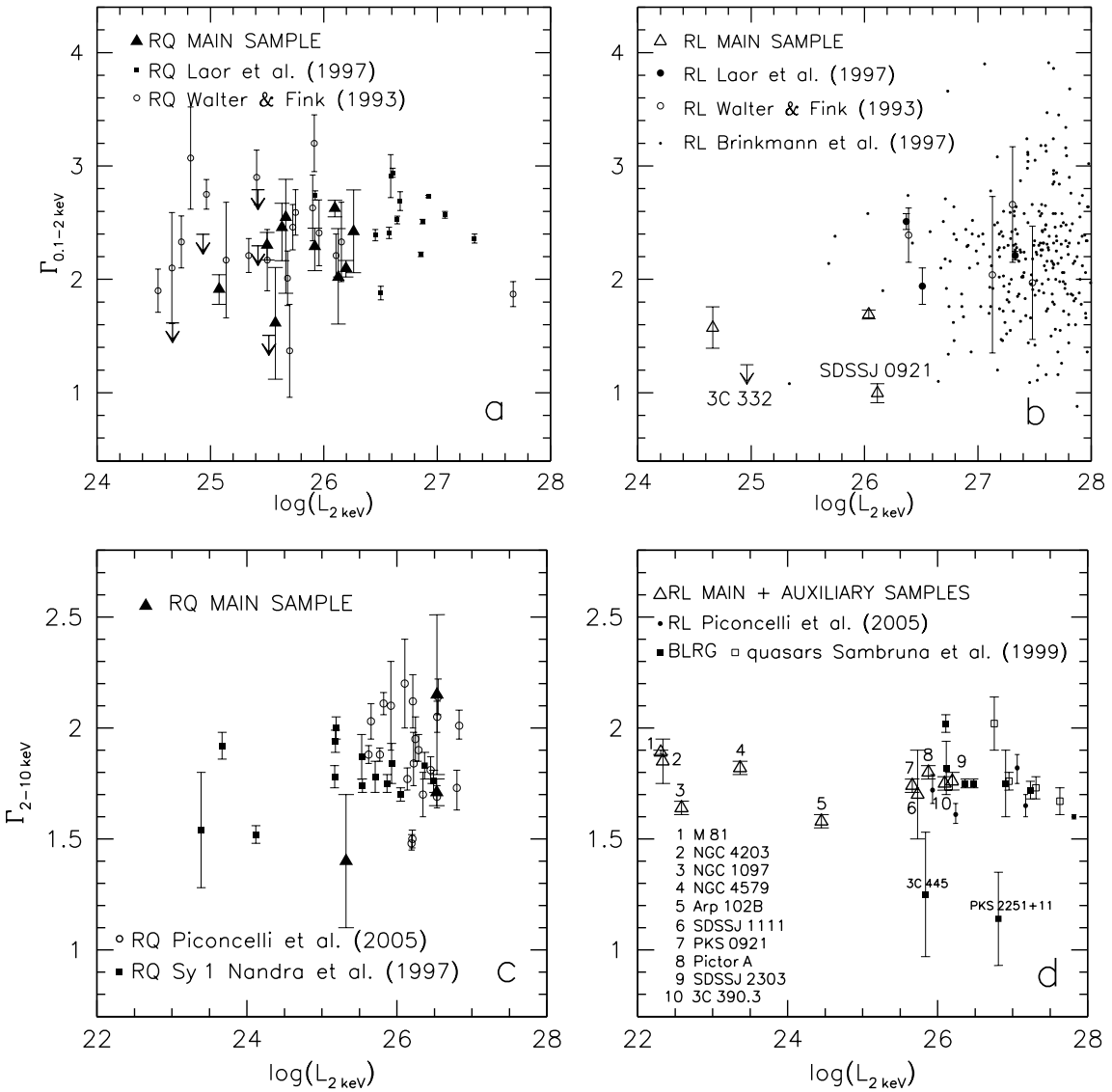

FIG. 10.— The 0.1–2 keV (panels a and b) and 2–10 keV (panels c and d) power-law slopes of RQ (a and c) and RL (b and d) double-peaked emitters in comparison with other broad-line AGN. The 0.1–2 keV power-law slopes were obtained using the standard *ROSAT* hardness ratio HR1, and the 2–10 keV power-law slopes were obtained through direct spectral fits. Arrows indicate upper limits on Γ (i.e., these AGN were not detected in the soft [0.1–0.41 keV] band). The two objects in the lower-right corner of panel d (PKS 2251+11 and 3C 445) are known to have large intrinsic absorbing column densities of $> 10^{22}\,\mathrm{cm}^{-2}$.

line AGN ($\mathrm{FWHM}_{\mathrm{H}\beta} > 2000\,\mathrm{km\,s}^{-1}$) were selected for this comparison, since some Narrow-Line Seyfert 1s are known to have exceptionally steep X-ray spectral slopes (e.g., Brandt & Boller 1999), and their inclusion could bias the results. From Figure 10, the X-ray spectral shapes of double-peaked emitters appear similar to those of normal AGN, except for the four RL double-peaked emitters in panel b. A one-dimensional K-S test confirms this statement for the hard-band power-law slopes shown in Figure 10d ($D = 0.18$, $P = 98\%$). There are only three hard-band photon index measurements for RQ double-peaked emitters in Figure 10c; consequently the K-S test results ($D = 0.5$, $P = 26\%$) might not be robust. A simple Student's t-test confirms that the means of the hard-band photon index distributions for the RQ double-peaked emitters and normal AGN are consistent, with $t = 0.7$ and $P = 51\%$.

The presence of photon-index upper limits in panels a and b of Figure 10 requires the use of the logrank, Gehan, or Peto & Prentice comparison tests. Since the comparison samples do not have censored data, while the double-peaked emitters do, the Peto & Prentice test should give the cleanest results, as it is less vulnerable to different censoring distributions than the logrank or Gehan tests (Feigelson & Nelson 1985). According to a Peto & Prentice test, the four RL double-peaked emitters in Figure 10b, with a K-M estimator mean of $\langle\Gamma\rangle = 1.3$ and a dispersion of $\sigma = 0.2$ (compared to $\langle\Gamma\rangle = 2.22$ and $\sigma = 0.04$ for the normal AGN), are significantly different from the normal AGN ($T = 4.8$, $P = 0\%$). As in the case for 3C 332 (see discussion below), this could be an indication of the presence of intrinsic absorption. Alternatively,

it may signify weaker soft excess, which is expected for the lowest Eddington-ratio AGN (which might lack optically thick emission from the innermost parts of the accretion disk). According to a Peto & Prentice test, the soft-band photon indices of the 15 double-peaked emitters in Figure 10a are significantly different from the comparison AGN ($T = 2.4$, $P = 2\%$). The evidence for this difference is however very weak, relying on the two double-peaked emitters with the flattest values of Γ, both of which are limits. If these two double-peaked emitters are removed from the comparison, the Peto & Prentice test gives a 8% probability that the remaining double-peaked emitters are indistinguishable from the normal AGN.

The estimates of the spectral shapes in the *ROSAT* band, which are based on hardness ratios, depend sensitively on the assumption that the double-peaked emitters have no intrinsic absorption above the Galactic values. As reported in § 3.2, we saw no evidence of intrinsic absorption in four of the seven main-sample double-peaked emitters. The remaining three cases (SDSSJ 918+5139, SDSSJ 0938+0057, and SDSSJ 1111+4820) show good evidence of intrinsic absorption, but the $N_{\rm H,intr}$ estimates are not robust, owing to the small number of counts available and the degeneracy between intrinsic absorption and spectral index in these cases. The prototype double-peaked emitter Arp 102B, has a confirmed intrinsic absorbing column, equivalent to $N_{\rm H,intr} = (2.8\pm0.3)\times 10^{21}\,{\rm cm}^{-2}$ (Eracleous et al. 2003). In fact, significant intrinsic neutral absorbing columns are a general characteristic of nearby BLRG (see Figure 6 of Sambruna et al. 1999). It is therefore plausible that the very hard power-law slope estimates obtained for some double-peaked emitters from the observed hardness ratios are a result of intrinsic absorption that was not taken into account. For example, SDSSJ 1617+3222 (3C 332), one of the six double-peaked emitters with power-law slope upper limits, has HR1> 0.6, which, for a Galactic obscuration of $N_H = 2\times10^{20}\,{\rm cm}^{-2}$ corresponds to $\Gamma \lesssim 1.2$. The 3C 332 *ROSAT* observation was previously studied by Crawford & Fabian (1994), who conclude that the hard spectral slope obtained by assuming Galactic absorption is probably an indication of an intrinsic absorber. Assuming $\Gamma = 1.8$, Crawford & Fabian (1994) derive an obscuring column of $N_{\rm H,intr} \approx 1\times10^{21}\,{\rm cm}^{-2}$. The UV-to-X-ray spectral-index of 3C 332 is $\alpha_{\rm ox} = -1.53$, while the value expected for a RL AGN with comparable UV monochromatic luminosity is ≈ -1.15[10], indicative of weaker X-ray emission than expected and suggestive of intrinsic absorption.

There are a total of four double-peaked emitters in panels a and b of Figure 10 with lower $\Gamma_{0.1-2\,{\rm keV}}$ than expected, two RL AGN (3C 332 and SDSSJ 0921+4538) with $\Gamma_{0.1-2\,{\rm keV}} < 1.5$, and two RQ AGN (SDSSJ 1101+5122 and SDSSJ 1150+0208) with $\Gamma_{0.1-2\,{\rm keV}}$ upper limits ($\lesssim 1.6$). The two RQ double-peaked emitters with low $\Gamma_{0.1-2\,{\rm keV}}$ upper limits have $\alpha_{\rm ox}$ values consistent within 0.05 with the Steffen et al. (2006) $\alpha_{\rm ox}$-$l_{2500\,\text{Å}}$ relation (indicating no intrinsic absorption), while SDSSJ 0921+4538 has $\alpha_{\rm ox} = -0.9$, with an expected value of $\alpha_{\rm ox} = -1.08$ (indicating $\sim 3\times$ stronger X-ray emission than expected and no intrinsic absorption). Taking into account the fact that three of the four double-peaked emitters with lower than expected $\Gamma_{0.1-2\,{\rm keV}}$ upper limits have small numbers of counts and only 0.5–2 keV-band detections, and that the observed scatter in the $\alpha_{\rm ox}$-$l_{2500\,\text{Å}}$ relation (~ 0.11, Strateva et al. 2005), we consider the above results, with the exception of those for 3C 332, to be inconclusive. Longer observations are necessary to measure accurately the power-law slopes and intrinsic absorption columns for double-peaked emitters with unusually low spectral index estimates in the 0.1–2 keV band.

[10] Assuming that RL AGN are on the average three times brighter at 2 keV than RQ AGN with comparable UV monochromatic luminosity.

4. ENERGY BUDGET

Using the inner (ξ_1) and outer (ξ_2) radii of the Hα emission region we can estimate the amount of energy available locally in the disk due to viscous stresses and compare it to the luminosity of the Hα line. An Hα-line luminosity of 10–20% or more of the locally available energy suggests the need for an external source of illumination. Assuming a standard Shakura & Sunyaev (1973) disk, Chen, Halpern, & Filippenko (1989) and Eracleous & Halpern (1994) estimate the gravitational power output of the line emitting disk annulus:

$$W_{\rm disk}(\xi_1,\xi_2) = 7.7\times10^{43} L_{X,42} \times \left[\frac{1}{\xi_1}\left(1-\sqrt{\frac{8}{3\xi_1}}\right) - \frac{1}{\xi_2}\left(1-\sqrt{\frac{8}{3\xi_2}}\right)\right] {\rm erg\,s^{-1}} \quad (1)$$

where $L_{X,42}$ is the 0.5–2 keV X-ray luminosity in units of $10^{42}\,{\rm erg\,s^{-1}}$, and we assume for the bolometric luminosity, $L_{\rm bol}$, $L_{\rm X}/L_{\rm bol} \approx 0.1$ and, for an accretion rate $\dot{M}$, $L_{\rm bol} = \zeta\dot{M}c^2$, with the efficiency for conversion of energy into radiation $\zeta \approx 0.1$. The Hα-line luminosities together with $L_{X,42}$ are listed in Table 1. Since only six objects admit axisymmetric-disk profile fits, and only these allow unique estimates of the emitting region, we have no direct measurements of ξ_1 and ξ_2 for each AGN in the main sample. We do know that the main sample studied here is representative of the S03 sample and that most circular or elliptical double-peaked emitters have inner-emission radii of $200\,R_G < \xi_1 < 1000\,R_G$ and outer-emission radii of $1000\,R_G < \xi_2 < 10000\,R_G$. SDSSJ 0942+0900 (Wang et al. 2005), is an exception, with robust inner radius estimates $\xi_1 \approx 80-100\,R_G$. Based on both observational (as noted above) and theoretical (the temperature of the disk increases for small ξ and will likely ionize all hydrogen, preventing Hα-line emission) arguments, it is safe to state that $\xi_1 > 80\,R_G$ for all known Balmer-line double-peaked emitters. For the average double-peaked emitter studied by S03, Strateva et al. (2006, in preparation) and Eracleous & Halpern (2003) find $\xi_1 \approx 450\,R_G$ and $\xi_2 \approx 3000\,R_G$.

Using the general sample constraints on ξ_1 and ξ_2 given above, we can now estimate $W_{\rm disk}$ from eqn. 1 for the 23 double-peaked emitters without axisymmetric-disk fits. Figure 11 shows the results assuming a typical double-peaked emitter with $\xi_1 \approx 450\,R_G$ and $\xi_2 \approx 3000\,R_G$ for each of the 23 objects (i.e., $W_{\rm disk} \approx 0.12\times10^{42} L_{X,42}\,{\rm erg\,s^{-1}}$). Only two of the 29 ($\sim 7\%$) double-peaked emitters would generate enough power locally

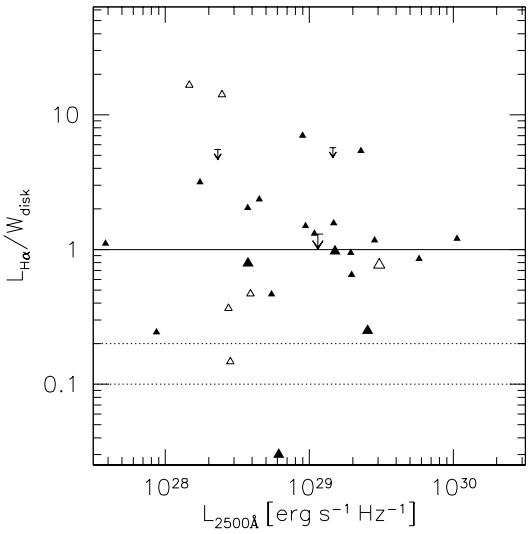

FIG. 11.— Rest-frame UV monochromatic luminosity vs. the ratio of the Hα line luminosity ($L_{\rm H\alpha}$) and the power available locally in the accretion disk ($W_{\rm disk}$). Open (filled) symbols indicate RL (RQ) AGN, arrows indicate the three upper limits. The larger symbols of each type denote the six AGN with direct estimates of the Hα-emission region and $W_{\rm disk}$ from circular disk fits; the smaller symbols indicate $W_{\rm disk}$ estimates which assume typical inner and outer emission radii, $\xi_1 \approx 450\,R_G$ and $\xi_2 \approx 3000\,R_G$. The dotted lines denote $L_{\rm H\alpha}/W_{\rm disk} = 10\%$ and 20%, while the solid line indicates $L_{\rm H\alpha} = W_{\rm disk}$. Note that in 16 of the 29 cases $L_{\rm H\alpha} > W_{\rm disk}$, i.e. local viscous dissipation in the disk cannot power the Hα line emission even in principle.

to produce Hα lines of the observed strength (assuming that as much as 20% of the power were radiated in the Hα line). Under the above assumptions for the extent of the emission region, the Hα line luminosity in fact exceeds the power produced locally in the disk in 16 of the 29 cases. Even if all double-peaked emitters without axisymmetric-disk fits had $\xi \approx 80\,R_G$ (and $\xi_2 \gtrsim 1000\,R_G$), $W_{\rm disk} \lesssim 0.77 \times 10^{42} L_{\rm X,42}\,{\rm erg\,s^{-1}}$; i.e., at most 13 out of the 29 ($\sim 45\%$) have enough energy generated locally to produce Hα lines of the observed strength. We conclude that the majority of double-peaked emitters require external illumination of the disk to account for the strength of the observed Hα line emission.

5. SUMMARY AND CONCLUSIONS

We have studied the X-ray emission properties of 39 AGN with double-peaked Hα lines, serendipitously observed by *ROSAT*, *XMM-Newton*, and *Chandra*, controlling for their UV and radio emission. The main sample consists of 29 objects selected from the SDSS which are representative of the sample of double-peaked emitters studied by S03. The remaining 10 objects (the auxiliary sample) are the best-studied double-peaked emitters (eight low optical-luminosity BLRG and LINER galaxies, and two RL quasars) with targeted and serendipitous X-ray observations. The total sample includes 16 RL and 23 RQ double-peaked emitters.

Based on a comparison of the UV-to-X-ray index, $\alpha_{\rm ox}$, we find that RQ double-peaked emitters as a class have comparable X-ray emission levels to those of normal RQ AGN of similar UV luminosity. RL double-peaked emitters tend to be brighter in the X-ray band in comparison with similar-luminosity normal RQ AGN, as observed for RL AGN in general. The 0.5–10 keV spectral shapes of the double-peaked emitters studied here are consistent with those of normal broad-line AGN with similar radio-loudness, with the possible exception of four RL double-peaked emitters with unusually flat soft-band spectra. Three double-peaked emitters observed above 2 keV show signs of large intrinsic absorption ($N_{\rm H,intr} \gtrsim 10^{22}\,{\rm cm^{-2}}$ in two of the three cases).

The majority of the double-peaked emitters require external illumination of the accretion disk, as the power generated locally is insufficient to produce lines of the observed strength. This result is more general and was used as an argument against the accretion-disk origin of broad emission lines in AGN, irrespective of their profiles (e.g., Collin-Souffrin et al. 1980). For AGN in which the Balmer-lines are double-peaked, this external illumination could be associated with an elevated structure in the inner disk (e.g., an X-ray emitting corona, jet, or vertically extended torus). However, the fact that the X-ray emission of double-peaked emitters as a class does not differ from that of normal AGN with similar properties, suggests that a peculiarity of the X-ray emission structure and/or mechanism is not responsible for the occurrence of double-peaked Balmer lines in AGN. Despite the importance of X-ray illumination for the majority of double-peaked emitters, the strength of the X-ray emission relative to the optical and UV emission cannot be used to predict if the broad, low-ionization lines are double-peaked. By extension, the structure of the inner disk is unlikely to be the only (or the dominant) reason for the observed double-peaked profiles.

Given the fact that double-peaked emitters as a class appear indistinguishable in their X-ray properties from normal AGN, the best course for the future might be to study in detail extreme cases of double-peaked emitters. Our upcoming *Chandra* observations, for example, include one of the most luminous known double-peaked emitters – an AGN with a double-peaked Mg II line. In addition, we hope to obtain high-quality hard-band X-ray observations of the broadest double-peaked Hα-line emitters, for which the emission region of the disk is likely to be in the immediate vicinity or even coincident with the X-ray emitting structure.

Acknowledgments

IVS, WNB and DPS acknowledge the support of NASA LTSA grant NAG5-13035. DPS acknowledges the support of NSF grant AST03-07582.

Funding for the SDSS and SDSS-II has been provided by the Alfred P. Sloan Foundation, the Participating Institutions, the National Science Foundation, the U.S. Department of Energy, the National Aeronautics and Space Administration, the Japanese Monbukagakusho, the Max Planck Society, and the Higher Education Funding Council for England. The SDSS Web Site is http://www.sdss.org/. The SDSS is managed by the Astrophysical Research Consortium for the Participating Institutions. The Participating Institutions are the American Museum of Natural History, Astrophysical Institute Potsdam, University of Basel, Cambridge

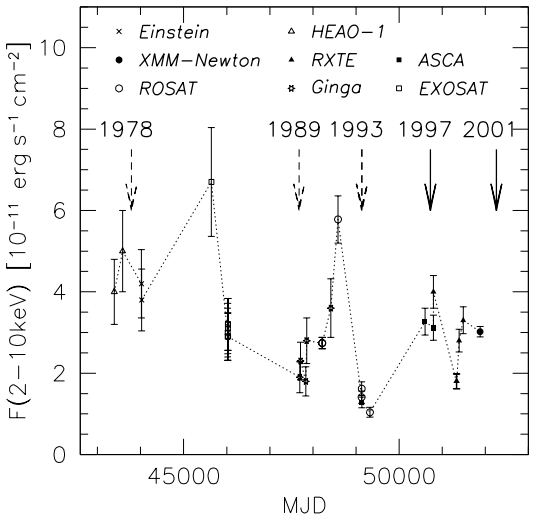

FIG. 12.— The 2–10 keV band variability of SDSSJ 2304−0841 (MCG-2-58-22, following Choi et al. 2002). The solid arrows indicate two optical spectra with double-peaked Balmer line profiles (obtained in 1997 and 2001), the dashed arrows indicate three optical spectra with single-peaked lines (obtained in 1978, 1989, and 1993; Durret & Bergeron 1988; Marziani et al. 2003; Argote et al. 2001).

University, Case Western Reserve University, University of Chicago, Drexel University, Fermilab, the Institute for Advanced Study, the Japan Participation Group, Johns Hopkins University, the Joint Institute for Nuclear Astrophysics, the Kavli Institute for Particle Astrophysics and Cosmology, the Korean Scientist Group, the Chinese Academy of Sciences (LAMOST), Los Alamos National Laboratory, the Max-Planck-Institute for Astronomy (MPA), the Max-Planck-Institute for Astrophysics (MPIA), New Mexico State University, Ohio State University, University of Pittsburgh, University of Portsmouth, Princeton University, the United States Naval Observatory, and the University of Washington.

This research has made use of the Tartarus (Version 3.1) database, created by Paul O'Neill and Kirpal Nandra at Imperial College London, and Jane Turner at NASA/GSFC. Tartarus is supported by funding from PPARC, and NASA grants NAG5-7385 and NAG5-7067. This research has made use of the NASA/IPAC Extragalactic Database (NED) which is operated by the Jet Propulsion Laboratory, California Institute of Technology, under contract with the National Aeronautics and Space Administration.

APPENDIX

THE X-RAY AND OPTICAL VARIABILITY OF SDSSJ 2304−0841

SDSSJ 2304−0841 is highly variable on long timescales (6–20 years). Choi et al. (2002) cite evidence of secular changes in flux accompanied by strong, shorter lived (∼1–2 years) flares[11]. Figure 12 shows the 2–10 keV band variability (following closely[12] Figure 1 of Choi et al. (2002)) with arrows indicating whether the Hα-line profiles were single or double-peaked. The 2002 optical SDSS observation shows complex Hα and Hβ line profiles with at least two peaks and an extended red tail. A 1997 observation by Argote et al. (2001) shows simple double-peaked profiles for both Balmer lines, while a May 1993 observation of Hβ by Marziani et al. (2003) and a 1989 observation by Argote et al. (2001) show simple single-peaked profiles characteristic of normal AGN. The earliest known optical spectrum of SDSSJ 2304−0841 was taken in 1978 by Durret & Bergeron (1988); judging by the spectrum in that paper the Hβ line was single peaked. The 1997 observation of a double-peaked Hα line coincides with one of the X-ray flares identified by Choi et al. (2002), while the three observations of single-peaked Hα lines are in non-flare regions according to Choi et al. (2002); we have no X-ray data coincident with the SDSS double-peaked profile (the *XMM-Newton*/*BeppoSAX* data were taken one year before the SDSS optical spectrum). From Figure 12 it is tempting to conclude that the occurrence of disk emission in the optical is unrelated to flares in the X-ray flux. This result, however, is highly uncertain, considering the sparse sampling time, the different X-ray bands observed, and the (significant) uncertainties of instrument cross-calibration. What is obvious from Figure 12, is that the appearance of optical double-peaked lines in not predominantly associated with either low- or high-X-ray-flux states. The X-ray spectral analysis presented in § 3.2.7 further suggests that the appearance of optical double-peaked lines is not correlated with the steepness of the hard-band spectrum or the presence of a strong Fe Kα line.

REFERENCES

Abazajian, K., et al. 2005, AJ, 129, 1755
Argote, M., Dultzin-Hyacyan, D., de Diego, J. A., et al. 2001, "Advanced Lectures on the Starburst-AGN Connection," Eds. R. Mujica, I. Aretxaga, & D. Knuth[13]
Barth, A. J., Ho, L. C., Filippenko, A. V., & Sargent, W. L. W. 1998, ApJ, 496, 133
Barth, A. J., Reichert, G. A., Filippenko, A. V., Ho, L. C., Shields, J. C., Mushotzky, R. F., & Puchnarewicz, E. M. 1996, AJ, 112, 1829
Bianchi, S., Matt, G., Balestra, I., Guainazzi, M., & Perola, G. C. 2004, A&A, 422, 65
Blandford, R. D., & Begelman, M. C. 1999, MNRAS, 303, L1
Brandt, W. N., & Boller, T. 1999, ASP Conf. Ser. 175: Structure and Kinematics of Quasar Broad Line Regions, 175, 265
Brinkmann, W., Yuan, W., & Siebert, J. 1997, A&A, 319, 413
Chen, K., Halpern, J. P., & Filippenko, A. V. 1989, ApJ, 339, 742
Chen, K., & Halpern, J. P. 1989, ApJ, 344, 115
Choi, C.-S., Dotani, T., Chang, H.-Y., & Yi, I. 2002, Journal of Korean Astronomical Society, 35, 1
Collin-Souffrin, S., Joly, M., Dumont, S., & Heidmann, N. 1980, A&A, 83, 190
Crawford, C. S., & Fabian, A. C. 1994, MNRAS, 266, 669
Dewangan, G. C., Griffiths, R. E., Di Matteo, T., & Schurch, N. J. 2004, ApJ, 607, 788
Durret, F., & Bergeron, J. 1988, A&AS, 75, 273
Eracleous, M., & Halpern, J. P. 1994, ApJS, 90, 1

[13] http://www.inaoep.mx/∼agn00/posters.html

[11] Choi et al. (2002) were interested in the X-ray flux variability only; they do not discuss the spectral shape and Fe-Kα variability or their relation to the variability in the optical line profile.

[12] We include the latest *XMM-Newton* point, replace the *ROSAT* fluxes from Choi et al. 2002 with our estimates, and the *ASCA* fluxes with the latest Tartarus database results obtained from HEASARC.

Eracleous, M., Shields, J. C., Chartas, G., & Moran, E. C. 2002, ApJ, 565, 108
Eracleous, M., Halpern, J. P., & Charlton, J. C. 2003, ApJ, 582, 633
Eracleous, M., & Halpern, J. P. 2003, ApJ, 599, 886
Feigelson, E. D. & Nelson, P. I. 1985, ApJ, 293, 192
Fleming, T. R., O'Fallon, J. R., O'Brien, P. C. & Harrington, D. P. 1980, Biometrics, 36, 607
Ho, L. C., Filippenko, A. V., & Sargent, W. L. W. 1996, ApJ, 462, 183
Ho, L. C., et al. 2001, ApJ, 549, L51
Isobe, T., Feigelson, E. D., & Nelson, P. I. 1986, ApJ, 306, 490
Iyomoto, N., Makishima, K., Matsushita, K., Fukazawa, Y., Tashiro, M., & Ohashi, T. 1998, ApJ, 503, 168
Ishisaki, Y., et al. 1996, PASJ, 48, 237
Kuiper, N. H. 1960, Proc. of the Koninkl. Nederl. Akad. van Wetenschappen, Ser. A., 63, 38 M., & Aldcroft, T. L. 2004, ApJS, 150, 165
Laor, A., Fiore, F., Elvis, M., Wilkes, B. J., & McDowell, J. C. 1997, ApJ, 477, 93
Latta, R. B. 1981, J. Am. Statistical Association, 26, 713
Lavalley, M., Isobe, T., & Feigelson, E. 1992, ASP Conf. Ser. 25: Astronomical Data Analysis Software and Systems I, 1, 245
Lewis, K. T. & Eracleous, M. 2006, ApJ, 642, 711
Lyons, L. 1991, Data Analysis for Physical Science Students (Cambridge: Cambridge Univ. Press)
Magdziarz, P., & Zdziarski, A. A. 1995, MNRAS, 273, 837
Marziani, P., Sulentic, J. W., Zamanov, et al. 2003, ApJS, 145, 199
Murray, N., & Chiang, J. 1997, ApJ, 474, 91
Nagao, T., Murayama, T., Shioya, Y., & Taniguchi, Y. 2002, ApJ, 567, 73
Nandra, K., George, I. M., Mushotzky, R. F., et al. 1997, ApJ, 477, 602
Narayan, R., Mahadevan, R., & Quataert, E. 1998, Theory of Black Hole Accretion Disks, 148
Page, K. L., Reeves, J. N., O'Brien, P. T., et al. 2004, MNRAS, 353, 133
Page, M. J., Soria, R., Zane, S., et al. 2004, A&A, 422, 77
Peacock, J. A. 1983, MNRAS, 202, 615
Piconcelli, E., Jimenez-Bailón, E., Guainazzi, M., Schartel, N., et al. 2005, A&A, 432, 15
Proga, D., Stone, J. M., & Kallman, T. R. 2000, ApJ, 543, 686
Sambruna, R. M., Eracleous, M., & Mushotzky, R. F. 1999, ApJ, 526, 60
Schneider, D. P., et al. 2005, AJ, 130, 367
Seaton, M. J. 1979, MNRAS, 187, 73P
Shakura, N. I. & Sunyaev, R. A. 1973, A&A, 24, 337
Spergel, D. N., et al. 2003, ApJS, 148, 175
Steffen, A., et al. 2006, AJ, submitted
Storchi-Bergmann, T., et al. 2003, ApJ, 598, 956
Strateva, I. V., et al. 2003, AJ, 126, 1720
Strateva, I. V., Brandt, W. N., Schneider, D. P., et al. 2005, AJ, 130, 387
Sulentic, J. W., Marziani, P., Zwitter, T., & Calvani, M. 1995, ApJ, 438, L1
Terashima, Y., Kunieda, H., Misaki, K., Mushotzky, R. F., Ptak, A. F., & Reichert, G. A. 1998, ApJ, 503, 212
Terashima, Y., Ho, L. C., Ptak, A. F., Yaqoob, T., Kunieda, H., Misaki, K., & Serlemitsos, P. J. 2000, ApJ, 535, L79
Terashima, Y., Kunieda, H., Misaki, K., Mushotzky, R. F., Ptak, A. F., & Reichert, G. A. 1998, ApJ, 503, 212
York, D. G., et al. 2000, AJ, 120, 1579
Vanden Berk, D. E., et al. 2001, AJ, 122, 549
Vanden Berk, D. E., et al. 2006, AJ, 131, 84
Vignali, C., Brandt, W. N., Schneider, D. P., & Kaspi, S. 2005, AJ, 129, 2519
Voges, W. 1993, Advances in Space Research, 13, 391
Walter, R., & Fink, H. H. 1993, A&A, 274, 105
Wang, T.-G., Dong, X.-B., Zhang, X.-G., et al. 2005, ApJ, 625, L35
Weaver, K. A., Nousek, J., Yaqoob, T., Hayashida, K., & Murakami, S. 1995, ApJ, 451, 147
Weaver, K. A., Gelbord, J., & Yaqoob, T. 2001, ApJ, 550, 261
Worrall, D. M., Tananbaum, H., Giommi, P., & Zamorani, G. 1987, ApJ, 313, 596
Wu, X.-B., & Liu, F. K. 2004, ApJ, 614, 91